EUROPEAN ORGANIZATION FOR NUCLEAR RESEARCH

CERN-PH-EP/2004-039
27th July, 2004

Flavour Independent h^0A^0 Search and Two Higgs Doublet Model Interpretation of Neutral Higgs Boson Searches at LEP

The OPAL Collaboration

Abstract

Upper limits on the cross-section of the pair-production process $e^+e^-\rightarrow h^0A^0$, assuming 100 % decays into hadrons, are derived from a new search for the $h^0A^0\rightarrow$ hadrons topology, independent of the hadronic flavour of the decay products. Searches for the neutral Higgs bosons h^0 and A^0, are used to obtain constraints on the Type II Two Higgs Doublet Model (2HDM(II)) with no CP violation in the Higgs sector and no additional non Standard Model particles besides the five Higgs bosons. The analysis combines LEP1 and LEP2 data collected with the OPAL detector up to the highest available centre-of-mass energies. The searches are sensitive to the h^0, $A^0\rightarrow q\bar{q}$, gg, $\tau^+\tau^-$ and $h^0\rightarrow A^0A^0$ decay modes of the Higgs bosons. The 2HDM(II) parameter space is explored in a detailed scan. Large regions of the 2HDM(II) parameter space are excluded at the 95% CL in the (m_h, m_A), (m_h, $\tan\beta$) and (m_A, $\tan\beta$) planes, using both direct neutral Higgs boson searches and indirect limits derived from Standard Model high precision measurements. The region $1 \lesssim m_h \lesssim 55$ GeV and $3 \lesssim m_A \lesssim 63$ GeV is excluded at 95 % CL independent of the choice of the 2HDM(II) parameters.

(Submitted to European Pysical Journal C)

The OPAL Collaboration

G. Abbiendi[2], C. Ainsley[5], P.F. Åkesson[3,y], G. Alexander[22], J. Allison[16], P. Amaral[9], G. Anagnostou[1], K.J. Anderson[9], S. Asai[23], D. Axen[27], I. Bailey[26], E. Barberio[8,p], T. Barillari[32], R.J. Barlow[16], R.J. Batley[5], P. Bechtle[25], T. Behnke[25], K.W. Bell[20], P.J. Bell[1], G. Bella[22], A. Bellerive[6], G. Benelli[4], S. Bethke[32], O. Biebel[31], O. Boeriu[10], P. Bock[11], M. Boutemeur[31], S. Braibant[2], R.M. Brown[20], H.J. Burckhart[8], S. Campana[4], P. Capiluppi[2], R.K. Carnegie[6], A.A. Carter[13], J.R. Carter[5], C.Y. Chang[17], D.G. Charlton[1], C. Ciocca[2], A. Csilling[29], M. Cuffiani[2], S. Dado[21], A. De Roeck[8], E.A. De Wolf[8,s], K. Desch[25], B. Dienes[30], M. Donkers[6], J. Dubbert[31], E. Duchovni[24], G. Duckeck[31], I.P. Duerdoth[16], E. Etzion[22], F. Fabbri[2], P. Ferrari[8], F. Fiedler[31], I. Fleck[10], M. Ford[16], A. Frey[8], P. Gagnon[12], J.W. Gary[4], C. Geich-Gimbel[3], G. Giacomelli[2], P. Giacomelli[2], M. Giunta[4], J. Goldberg[21], E. Gross[24], J. Grunhaus[22], M. Gruwé[8], P.O. Günther[3], A. Gupta[9], C. Hajdu[29], M. Hamann[25], G.G. Hanson[4], A. Harel[21], M. Hauschild[8], C.M. Hawkes[1], R. Hawkings[8], R.J. Hemingway[6], G. Herten[10], R.D. Heuer[25], J.C. Hill[5], K. Hoffman[9], D. Horváth[29,c], P. Igo-Kemenes[11], K. Ishii[23], H. Jeremie[18], P. Jovanovic[1], T.R. Junk[6,i], J. Kanzaki[23,u], D. Karlen[26], K. Kawagoe[23], T. Kawamoto[23], R.K. Keeler[26], R.G. Kellogg[17], B.W. Kennedy[20], S. Kluth[32], T. Kobayashi[23], M. Kobel[3], S. Komamiya[23], T. Krämer[25], P. Krieger[6,l], J. von Krogh[11], T. Kuhl[25], M. Kupper[24], G.D. Lafferty[16], H. Landsman[21], D. Lanske[14], D. Lellouch[24], J. Letts[o], L. Levinson[24], J. Lillich[10], S.L. Lloyd[13], F.K. Loebinger[16], J. Lu[27,w], A. Ludwig[3], J. Ludwig[10], W. Mader[3,b], S. Marcellini[2], A.J. Martin[13], G. Masetti[2], T. Mashimo[23], P. Mättig[m], J. McKenna[27], R.A. McPherson[26], F. Meijers[8], W. Menges[25], F.S. Merritt[9], H. Mes[6,a], N. Meyer[25], A. Michelini[2], S. Mihara[23], G. Mikenberg[24], D.J. Miller[15], W. Mohr[10], T. Mori[23], A. Mutter[10], K. Nagai[13], I. Nakamura[23,v], H. Nanjo[23], H.A. Neal[33], R. Nisius[32], S.W. O'Neale[1,*], A. Oh[8], M.J. Oreglia[9], S. Orito[23,*], C. Pahl[32], G. Pásztor[4,g], J.R. Pater[16], J.E. Pilcher[9], J. Pinfold[28], D.E. Plane[8], O. Pooth[14], M. Przybycień[8,n], A. Quadt[3], K. Rabbertz[8,r], C. Rembser[8], P. Renkel[24], J.M. Roney[26], A.M. Rossi[2], Y. Rozen[21], K. Runge[10], K. Sachs[6], T. Saeki[23], E.K.G. Sarkisyan[8,j], A.D. Schaile[31], O. Schaile[31], P. Scharff-Hansen[8], J. Schieck[32], T. Schörner-Sadenius[8,z], M. Schröder[8], M. Schumacher[3], R. Seuster[14,f], T.G. Shears[8,h], B.C. Shen[4], P. Sherwood[15], A. Skuja[17], A.M. Smith[8], R. Sobie[26], S. Söldner-Rembold[16], F. Spano[9], A. Stahl[3,x], D. Strom[19], R. Ströhmer[31], S. Tarem[21], M. Tasevsky[8,s], R. Teuscher[9], M.A. Thomson[5], E. Torrence[19], D. Toya[23], P. Tran[4], I. Trigger[8], Z. Trócsányi[30,e], E. Tsur[22], M.F. Turner-Watson[1], I. Ueda[23], B. Ujvári[30,e], C.F. Vollmer[31], P. Vannerem[10], R. Vértesi[30,e], M. Verzocchi[17], H. Voss[8,q], J. Vossebeld[8,h], C.P. Ward[5], D.R. Ward[5], P.M. Watkins[1], A.T. Watson[1], N.K. Watson[1], P.S. Wells[8], T. Wengler[8], N. Wermes[3], G.W. Wilson[16,k], J.A. Wilson[1], G. Wolf[24], T.R. Wyatt[16], S. Yamashita[23], D. Zer-Zion[4], L. Zivkovic[24]

[1]School of Physics and Astronomy, University of Birmingham, Birmingham B15 2TT, UK
[2]Dipartimento di Fisica dell' Università di Bologna and INFN, I-40126 Bologna, Italy
[3]Physikalisches Institut, Universität Bonn, D-53115 Bonn, Germany

[4]Department of Physics, University of California, Riverside CA 92521, USA
[5]Cavendish Laboratory, Cambridge CB3 0HE, UK
[6]Ottawa-Carleton Institute for Physics, Department of Physics, Carleton University, Ottawa, Ontario K1S 5B6, Canada
[8]CERN, European Organisation for Nuclear Research, CH-1211 Geneva 23, Switzerland
[9]Enrico Fermi Institute and Department of Physics, University of Chicago, Chicago IL 60637, USA
[10]Fakultät für Physik, Albert-Ludwigs-Universität Freiburg, D-79104 Freiburg, Germany
[11]Physikalisches Institut, Universität Heidelberg, D-69120 Heidelberg, Germany
[12]Indiana University, Department of Physics, Bloomington IN 47405, USA
[13]Queen Mary and Westfield College, University of London, London E1 4NS, UK
[14]Technische Hochschule Aachen, III Physikalisches Institut, Sommerfeldstrasse 26-28, D-52056 Aachen, Germany
[15]University College London, London WC1E 6BT, UK
[16]Department of Physics, Schuster Laboratory, The University, Manchester M13 9PL, UK
[17]Department of Physics, University of Maryland, College Park, MD 20742, USA
[18]Laboratoire de Physique Nucléaire, Université de Montréal, Montréal, Québec H3C 3J7, Canada
[19]University of Oregon, Department of Physics, Eugene OR 97403, USA
[20]CCLRC Rutherford Appleton Laboratory, Chilton, Didcot, Oxfordshire OX11 0QX, UK
[21]Department of Physics, Technion-Israel Institute of Technology, Haifa 32000, Israel
[22]Department of Physics and Astronomy, Tel Aviv University, Tel Aviv 69978, Israel
[23]International Centre for Elementary Particle Physics and Department of Physics, University of Tokyo, Tokyo 113-0033, and Kobe University, Kobe 657-8501, Japan
[24]Particle Physics Department, Weizmann Institute of Science, Rehovot 76100, Israel
[25]Universität Hamburg/DESY, Institut für Experimentalphysik, Notkestrasse 85, D-22607 Hamburg, Germany
[26]University of Victoria, Department of Physics, P O Box 3055, Victoria BC V8W 3P6, Canada
[27]University of British Columbia, Department of Physics, Vancouver BC V6T 1Z1, Canada
[28]University of Alberta, Department of Physics, Edmonton AB T6G 2J1, Canada
[29]Research Institute for Particle and Nuclear Physics, H-1525 Budapest, P O Box 49, Hungary
[30]Institute of Nuclear Research, H-4001 Debrecen, P O Box 51, Hungary
[31]Ludwig-Maximilians-Universität München, Sektion Physik, Am Coulombwall 1, D-85748 Garching, Germany
[32]Max-Planck-Institute für Physik, Föhringer Ring 6, D-80805 München, Germany
[33]Yale University, Department of Physics, New Haven, CT 06520, USA

[a] and at TRIUMF, Vancouver, Canada V6T 2A3
[b] now at University of Iowa, Dept of Physics and Astronomy, Iowa, U.S.A.
[c] and Institute of Nuclear Research, Debrecen, Hungary
[e] and Department of Experimental Physics, University of Debrecen, Hungary
[f] and MPI München
[g] and Research Institute for Particle and Nuclear Physics, Budapest, Hungary
[h] now at University of Liverpool, Dept of Physics, Liverpool L69 3BX, U.K.
[i] now at Dept. Physics, University of Illinois at Urbana-Champaign, U.S.A.
[j] and Manchester University
[k] now at University of Kansas, Dept of Physics and Astronomy, Lawrence, KS 66045, U.S.A.
[l] now at University of Toronto, Dept of Physics, Toronto, Canada
[m] current address Bergische Universität, Wuppertal, Germany
[n] now at University of Mining and Metallurgy, Cracow, Poland
[o] now at University of California, San Diego, U.S.A.
[p] now at The University of Melbourne, Victoria, Australia
[q] now at IPHE Université de Lausanne, CH-1015 Lausanne, Switzerland
[r] now at IEKP Universität Karlsruhe, Germany
[s] now at University of Antwerpen, Physics Department,B-2610 Antwerpen, Belgium; supported by Interuniversity Attraction Poles Programme – Belgian Science Policy
[u] and High Energy Accelerator Research Organisation (KEK), Tsukuba, Ibaraki, Japan
[v] now at University of Pennsylvania, Philadelphia, Pennsylvania, USA
[w] now at TRIUMF, Vancouver, Canada
[x] now at DESY Zeuthen
[y] now at CERN
[z] now at DESY
[*] Deceased

1 Introduction

The data collected by the OPAL detector at LEP during the years 1999 and 2000 at centre-of-mass energies $\sqrt{s} \approx 192,\ 196,\ 200-209$ GeV are combined with the data at the Z^0 pole, $\sqrt{s} \approx 183$ GeV and 189 GeV, to search for neutral Higgs bosons [1–3] in the framework of the Type II Two Higgs Doublet Model (2HDM(II)) [4, 5] with no CP violation in the Higgs sector and no additional particles besides those arising from the Higgs mechanism. This study updates the results of a previous OPAL publication [6], which included data at the Z^0 pole, $\sqrt{s} \approx 183$ GeV and 189 GeV.

In the minimal Standard Model (SM) the Higgs sector comprises only one complex Higgs doublet [1] resulting in one physical neutral Higgs scalar whose mass is a free parameter of the theory. However, it is important to study extended models containing more than one physical Higgs boson in the spectrum. In particular, Two Higgs Doublet Models (2HDMs) are attractive extensions of the SM since they add new phenomena with the fewest new parameters; they satisfy the constraints of $\rho \approx 1$ [7] and the absence of tree-level flavour changing neutral currents, if the Higgs-fermion couplings are appropriately chosen.

In the context of 2HDMs the Higgs sector comprises five physical Higgs bosons: two neutral CP-even scalars, h^0 and H^0 (with $m_h < m_H$), one CP-odd scalar, A^0, and two charged scalars, $H^{\pm}$. The four Higgs masses are free parameters of the model.

Within 2HDMs the choice of the couplings between the Higgs bosons and the fermions determines the type of the model considered. In the Type II model the first Higgs doublet couples only to down–type fermions and the second Higgs doublet couples only to up–type fermions. In the Type I model the quarks and leptons only couple to the second Higgs doublet. The Higgs sector in the minimal supersymmetric extension of the SM [7, 8] is a Type II 2HDM, in which the introduction of supersymmetry adds new particles and constrains the parameter space of the Higgs sector of the model. The 2HDM(II) Higgs potential and detailed description of the physical parameters of the model are given in [4, 5, 7].

At the centre-of-mass energies accessed by LEP, the h^0 and A^0 bosons are expected to be produced predominantly via two processes: the *Higgs-strahlung* process $e^+e^- \to h^0Z^0$ and the *pair–production* process $e^+e^- \to h^0A^0$. The cross-sections for these two processes, σ_{hZ} and σ_{hA}, are related at tree-level to the SM Higgs-strahlung production cross-section by the following relations [7]:

$$e^+e^- \to h^0Z^0 : \quad \sigma_{hZ} = \sin^2(\beta-\alpha)\,\sigma^{SM}_{HZ}, \tag{1}$$

$$e^+e^- \to h^0A^0 : \quad \sigma_{hA} = \cos^2(\beta-\alpha)\,\bar{\lambda}\,\sigma^{SM}_{HZ}, \tag{2}$$

where σ^{SM}_{HZ} is the Higgs-strahlung cross-section for the SM process $e^+e^- \to H^0_{SM}Z^0$, α is the Higgs mixing angle, $\tan\beta$ is defined in terms of the ratio of the vacuum expectation values, v_1 and v_2, of the two scalar fields, $\tan\beta = v_2/v_1$ and $\bar{\lambda} = \lambda^{3/2}_{Ah}/\{\lambda^{1/2}_{Zh}[12m^2_Z/s + \lambda_{Zh}]\}$ accounts for the suppression of the P-wave cross-section near the threshold, with $\lambda_{ij} = (1-m^2_i/s+m^2_j/s)^2-4m^2_im^2_j/s^2$ being the two–particle phase–space factor.

In a 2HDM the production cross-sections and Higgs boson decay branching ratios are predicted for a given set of model parameters. The coefficients $\sin^2(\beta-\alpha)$ and $\cos^2(\beta-\alpha)$ which appear in Eqs. (1) and (2) determine the production cross-sections. The decay branching ratios to the various final states are also determined by α and β. In the 2HDM(II) the tree-level couplings of the h^0 and A^0 bosons to the up– and down–type quarks relative to the couplings of the SM Higgs boson to the corresponding fermions are [7]

$$\mathrm{h}^0\mathrm{c\bar{c}} : \frac{\cos\alpha}{\sin\beta}, \quad \mathrm{h}^0\mathrm{b\bar{b}} : -\frac{\sin\alpha}{\cos\beta}, \quad \mathrm{A}^0\mathrm{c\bar{c}} : \cot\beta, \quad \mathrm{A}^0\mathrm{b\bar{b}} : \tan\beta, \tag{3}$$

indicating the need for a scan over the range of both angles when considering the different production cross-section mechanisms and final state topologies.

In the analysis described in this paper, detailed scans over broad ranges of these parameters are performed. Each of the scanned points is considered as an independent scenario within the 2HDM(II), and results are provided for each point in the (m_h, m_A, tanβ, α) space. The masses m_h and m_A are varied such that the kinematically accessible range at LEP is fully covered. The choice $0 < \beta < \pi/2$ is derived from $v_1, v_2 > 0$ which in the MSSM implies that $-\pi/2 \leq \alpha \leq 0$ [9]. This range was studied in [6] to cover an MSSM oriented 2HDM(II). However, to completely cover any 2HDM(II), α has to be varied over an arbitrarily chosen angular range of π. In order to extend the analysis done in [6] beyond the MSSM–like 2HDM(II), the domain $-\pi/2 \leq \alpha \leq \pi/2$ is explored in the present study. The final-state topologies of the processes (1) and (2) are determined by the decays of the Z^0, h^0 and A^0 bosons. Higgs bosons couple to fermions with a strength proportional to the fermion mass, favouring the decays into pairs of b–quarks and tau leptons at LEP energies. However, with values of α and tanβ close to zero the decays into up–type light quarks and gluons through quark loops become dominant, motivating the inclusion of flavour independent analyses.

Section 2 contains a short description of the OPAL detector and the Monte Carlo simulations used. A new analysis at the highest LEP energies with improved sensitivity for the process $\mathrm{e}^+\mathrm{e}^-\rightarrow\mathrm{h}^0\mathrm{A}^0\rightarrow$ hadrons, independent of the hadronic flavour of the decay products, is presented in Section 3. In Section 4 the confidence level calculation method is described. A limit on the cross-section of the pair-production process $\mathrm{e}^+\mathrm{e}^-\rightarrow\mathrm{h}^0\mathrm{A}^0$, assuming 100 % decays into hadrons, is given in Section 5. The data samples, the final state topologies studied and the external constraints used for the 2HDM(II) interpretation are described in Section 6. The 2HDM(II) interpretation of the searches is presented in Section 7, and in Section 8 the results are summarised and conclusions are drawn.

2 OPAL detector and Monte Carlo samples

The OPAL detector [10] has nearly complete solid angle coverage and excellent hermeticity. The innermost detector of the central tracking is a high-resolution silicon microstrip vertex detector [11] which lies immediately outside of the beam pipe. The silicon microvertex detector is surrounded by a high precision vertex drift chamber, a large volume jet chamber, and z–chambers to measure the z coordinates[1] of tracks, all in a uniform 0.435 T axial magnetic field. The lead-glass electromagnetic calorimeter and the presampler are located outside the magnet coil. It provides,

---

[1] OPAL uses a right-handed coordinate system where the $+z$ direction is along the electron beam and where $+x$ points to the centre of the LEP ring. The polar angle, θ, is defined with respect to the $+z$ direction and the azimuthal angle, ϕ, with respect to the horizontal, $+x$ direction.

Year	$\sqrt{s}$ [GeV]	$\mathcal{L}$ [pb^{-1}]
1999	191.6	28.9
1999	195.5	74.8
1999	199.5	77.2
1999	201.6	36.1
2000	206.0	208

Table 1: The integrated luminosities, $\mathcal{L}$, at each centre-of-mass energy, $\sqrt{s}$, used for the flavour independent $\mathrm{h}^0\mathrm{A}^0\to$ hadrons search.

in combination with a number of forward detectors and the silicon-tungsten luminometer [12], geometrical acceptance down to 25 mrad from the beam direction. The silicon-tungsten luminometer serves to measure the integrated luminosity using small angle Bhabha scattering events [13]. The magnet return yoke is instrumented with streamer tubes and thin gap chambers for hadron calorimetry and is surrounded by several layers of muon chambers.

Events are reconstructed from charged particle tracks and energy deposits ("clusters") in the electromagnetic and hadron calorimeters. The tracks and clusters must pass a set of quality requirements similar to those used in previous OPAL Higgs boson searches [14]. Charged particle tracks and energy clusters, satisfying these requirements, are associated to form "energy flow objects". A matching algorithm is employed to reduce double counting of energy in cases where charged tracks point toward electromagnetic clusters [14]. The energy flow objects are then grouped into jets and contribute to the total energy and momentum of the event. The association into jets is performed by the Durham jet finder algorithm [15].

For the $\mathrm{h}^0\mathrm{A}^0\to$hadrons analysis, the data are separated into four $\sqrt{s}$ bins for the 1999 data, with average $\sqrt{s}$ values of approximately 192 GeV, 196 GeV, 200 GeV, and 202 GeV. All of the 2000 data is treated together, with an average $\sqrt{s}$ of 206 GeV. The luminosities of each of the five data samples are given in Table 1.

A variety of Monte Carlo samples has been generated in order to estimate the detection efficiencies for Higgs boson production and background from SM processes. Monte Carlo signal samples are generated using `HZHA` [16] on a grid in the (m_h, m_A) plane, as shown in Figure 1. One thousand signal Monte Carlo events are generated and simulated for each grid point for each of the five centre-of-mass energies given in Table 1. Samples are generated for four flavour combinations of the decays, $\mathrm{h}^0\mathrm{A}^0\to\mathrm{b\bar{b}b\bar{b}}$, $\mathrm{h}^0\mathrm{A}^0\to\mathrm{b\bar{b}c\bar{c}}$, $\mathrm{h}^0\mathrm{A}^0\to\mathrm{c\bar{c}c\bar{c}}$, and $\mathrm{h}^0\mathrm{A}^0\to$ gggg.

For the background processes the following event generators are used: `KK2f` [17] for $(\mathrm{Z}/\gamma)^*\to\mathrm{q\bar{q}}(\gamma)$, $\mu^+\mu^-(\gamma)$ and $\tau^+\tau^-(\gamma)$, `BHWIDE` [18] for $\mathrm{e}^+\mathrm{e}^-(\gamma)$ and `KORALW` [19] and `grc4f` [20] for four-fermion processes. The `KK2f` prediction for $\mathrm{q\bar{q}}(\gamma)$ were compared to `PYTHIA` [21] and `HERWIG` [22] samples. The `KORALW` prediction for hadronic and semi-leptonic four-fermion processes (with no electron in the final state) were compared to `grc4f` samples. `JETSET` [21] is used as the principal model for fragmentation.

The detector response to the generated particles is simulated in full detail [23].

3 Flavour independent search for $e^+e^-\rightarrow h^0A^0$

For some values of the parameters specifying a 2HDM(II), $e^+e^-\rightarrow h^0Z^0$ is suppressed, either kinematically or due to small $\sin^2(\beta-\alpha)$. The decays $h^0\rightarrow b\bar{b}$ and $A^0\rightarrow b\bar{b}$ may be also suppressed in a subset of these models because of reduced couplings. In such models, the largest signal for Higgs boson production may be $e^+e^-\rightarrow h^0A^0$ where both the h^0 and the A^0 decay hadronically, but not necessarily to $b\bar{b}$. The dominant decay modes of the Higgs bosons may even be to pairs of gluons. The final state investigated here is four well-separated jets of hadrons of any flavour.

The search presented here is based on the search procedure applied to the 189 GeV data [6]. The search is extended by including all data collected at $\sqrt{s}=192$ to 209 GeV, and by introducing a likelihood discriminant to combine information carried by several different kinematic variables which are measured in each event. The results of the search for $e^+e^-\rightarrow h^0A^0\rightarrow$ hadrons in [6] are combined with the results of the newer searches; the older data are not re-analysed.

Without flavour tagging, and without a fixed mass constraint such as the Z^0 mass, the assignment of dijets in selected candidate events to the h^0 and A^0 is ambiguous. There are six possible assignments of jets to bosons. The pairing chosen in this analysis is the same as that used in [6]. This is the pairing which minimizes the χ^2 of a beam energy and momentum-constrained kinematic fit to the (m_h, m_A) hypothesis under study. The pairing of each event therefore depends on the test masses.

The Standard Model backgrounds for $e^+e^-\rightarrow h^0A^0\rightarrow$ hadrons are large. One of the main sources is $e^+e^-\rightarrow q\bar{q}$ (approximately 18 pb for events with less than 20 % of the centre-of-mass energy in initial state radiation at $\sqrt{s}=205$ GeV [24]), and includes events which may have one or more initial-state-radiation photons. Much of this background has only two jets. Hard gluon radiation in a fraction of $e^+e^-\rightarrow q\bar{q}$ events produces four-jet final states. In general, the radiation of a gluon produces jets close in angle to other jets, and so this background tends to mimic $e^+e^-\rightarrow h^0A^0\rightarrow$ hadrons where either the h^0 or the A^0 is light. Conversely if both the h^0 and the A^0 are assumed to be light, then signal events are more two-jet-like, and closely resemble a larger fraction of the $q\bar{q}$ background. The other main source of background is the production of pairs of vector bosons which decay hadronically. The most important process is $e^+e^-\rightarrow W^+W^-\rightarrow$ hadrons (approximately 8 pb at $\sqrt{s}=205$ GeV [24]); the process $e^+e^-\rightarrow Z^0Z^{0(*)}\rightarrow$ hadrons contributes at a smaller level (approximately 0.5 pb at $\sqrt{s}=205$ GeV [24]). These background processes produce four-jet events with large invariant masses when jets are combined together in pairs. The W^+W^- background mimics a signal with $m_h\approx m_A\approx m_W$. Furthermore, because the pairing of jets to bosons is ambiguous, the W^+W^- and $Z^0Z^{0(*)}$ backgrounds can contribute everywhere in the (m_h, m_A) plane.

The event selection starts with a cut-based preselection and proceeds with a selection based on a likelihood function.

3.1 Preselection

The preselection is based on the preselection used in the search for the Standard Model Higgs boson in the Higgs-strahlung process in the four-jet final state [14], without the requirement that two jets are consistent with m_{Z}. The cuts are:

1. Events must satisfy the hadronic final-state requirement of [25]. The effective centre-of-mass energy, $\sqrt{s'}$, obtained by kinematic fits assuming that initial state radiation photons are lost in the beampipe or seen in the detector [25] must be at least 80 % of $\sqrt{s}$. The value of the jet resolution parameter, y_{34}, at which an event is reclassified from 3– to 4–jet event by the Durham algorithm [15] must exceed 0.003.

2. The C parameter, which gives a measure of the spherical shape of the event [26], must be larger than 0.25.

3. The χ^2 probability of a 4-constraint (4C) kinematic fit requiring energy and momentum conservation must be greater than 10^{-5}.

4. The event is forced to have four jets and each of the four jets must have at least one charged particle track.

5. No jet-pairing combination may have a 6-constraint (6C) kinematic fit probability greater than 0.2, where the fit constrains the total energy, momentum, and the masses of both dijets to $m_{\mathrm{W}^\pm}$.

Table 2 shows the numbers of events passing each of the preselection requirements in the data taken in 1999 and 2000, along with the expected backgrounds and the efficiency for a signal with $m_{\mathrm{h}} = 50$ GeV and $m_{\mathrm{A}} = 100$ GeV.

3.2 Likelihood Selection

The following nine kinematic variables were considered in the likelihood selection:

- $\log(\Delta\chi^2(m_{\mathrm{h}},\ m_{\mathrm{A}}))$. A full description of the procedure for computing this variable is given in [6], where it was used as the only discriminant variable. For each event, a 4C kinematic fit is performed, constraining the event energy and momentum to the centre-of-mass energy and momentum. The $\Delta\chi^2(m_{\mathrm{h}},\ m_{\mathrm{A}})$ value is the additional χ^2 incurred when constraining one pair of jets to have invariant mass m_{h} and the other to have m_{A}. The pairing is chosen to minimise $\Delta\chi^2(m_{\mathrm{h}},\ m_{\mathrm{A}})$. This is the only variable for which the value depends on the test mass combination.

- $|\cos\theta_{\mathrm{thrust}}|$, obtained from the polar angle, θ_{thrust}, of the thrust axis.

- The event aplanarity A.

- $\log(y_{34})$.

- The jet-angle sum J_s [27]. This variable is the sum of the four smallest dijet angles.

- $(E_{\mathrm{max}} - E_{\mathrm{min}})/\sqrt{s}$, the difference between the energy of the highest-energy jet and that of the lowest-energy jet, divided by the centre-of-mass energy.

- The jet-charge-signed $\cos\theta_{\mathrm{W}}$. This variable is computed using the jet pairing which maximizes the 6C fit probability to the $\mathrm{W}^+\mathrm{W}^-$ mass hypothesis. The quantity

  $$Q_j \;=\; \sum_{i=1}^{n_{\mathrm{tracks}}} q_i \;\mathrm{sign}(p^i_{\parallel})\sqrt{|p^i_{\parallel}|} \tag{4}$$

  is computed for each jet j, where n_{tracks} is the number of tracks in the jet, q_i is the charge of the ith track in the jet, and $p^i_{\parallel} \;=\; \vec{p_i}\cdot\hat{n}_j$ where $\vec{p_i}$ is the three-momentum of the ith track in the jet and $\hat{n}_j$ is the unit vector pointing along the jet axis. If jets j and k are paired together to form a W boson candidate and jets l and m are paired to form the other W boson candidate, then

  $$\cos\theta_{\mathrm{W}} \;=\; \frac{\left(\vec{P}_j+\vec{P}_k\right)\cdot\hat{z}}{\left|\vec{P}_j+\vec{P}_k\right|}\mathrm{sign}\left(Q_j+Q_k-Q_l-Q_m\right), \tag{5}$$

  where $\vec{P}_j$ is the three-momentum of the jet j after the 4C-fit and $\hat{z}$ is the unit vector pointing along the electron beam axis.

- $\log(W_{\mathrm{CC03}})$, the logarithm of the WW matrix element calculated by the `EXCALIBUR` program [28] using the CC03 set of diagrams. The four-vectors of the jets after the 4C-fit are used as inputs to the calculation. The matrix element is computed for all possible assignments of jet pairs to W bosons and the largest value is used.

- $\log(W_{\mathrm{QCD}})$, the logarithm of the $\mathrm{e}^+\mathrm{e}^-\rightarrow\mathrm{q}\bar{\mathrm{q}}\rightarrow$ four-jet matrix element [29]. The matrix element is computed for all possible permutations of jets and the largest value is used.

Reference histograms are formed for each likelihood input variable, for each signal grid point, separately for the $\mathrm{e}^+\mathrm{e}^-\rightarrow\mathrm{q}\bar{\mathrm{q}}$ background (2f), the $\mathrm{e}^+\mathrm{e}^-\rightarrow$ qqqq background (4f), and the expected signal, accumulating events which pass the preselection requirements. The $\ell^+\ell^-\mathrm{q}\bar{\mathrm{q}}$ and $\ell\nu_\ell\mathrm{qq}$ backgrounds are expected to be small after the preselection – their numbers are included in the 4f background numbers in Table 2. They do not contribute to the reference histograms, but are accounted for in the final background estimates in the likelihood output histograms. The backgrounds from two-photon processes are negligible after the preselection.

Figure 2 shows the distributions of the likelihood input variables for the data collected in 1999 and 2000, the corresponding background estimate, and the expected signal for a fully gluonic decay for the hypothesis $m_{\mathrm{h}} = 50$ GeV, $m_{\mathrm{A}} = 60$ GeV.

For any point in the $(m_{\mathrm{h}},\, m_{\mathrm{A}})$ plane within kinematic reach of the LEP beam energy, and with $m_{\mathrm{h}} > 30$ GeV and $m_{\mathrm{A}} > 30$ GeV, a separate likelihood function may be constructed from the reference histograms of the input variables. These are formed by interpolating the signal reference histograms using nearby Monte Carlo grid points. The background reference histograms must be interpolated also for the $\log(\Delta\chi^2(m_{\mathrm{h}},\; m_{\mathrm{A}}))$ variable. These interpolations make use of the method described in [30], extended to interpolate histograms which are functions of two variables, m_{h} and m_{A}. The likelihood output histograms are also interpolated, separately for the signal and each background contribution, but each bin's contents

Cut	2f bkg	4f bkg	tot bkg	data	eff [%]
(1)	1031.6	3206.4	4238.0	4479	76.6
(2)	976.0	3203.1	4179.1	4436	76.6
(3)	887.3	2977.2	3864.5	3807	71.0
(4)	784.7	2820.2	3605.0	3580	70.4
(5)	754.3	2035.7	2789.9	2835	68.5

Table 2: The numbers of events passing each of the preselection requirements in the data taken in 1999 and 2000, along with the expected backgrounds and the luminosity-weighted average efficiency for a signal with $m_{\mathrm{h}} = 50$ GeV, $m_{\mathrm{A}} = 100$ GeV.

is linearly interpolated between the Monte Carlo grid points. The interpolated reference histograms allow the computation of the value of the likelihood function for each candidate for each point in the $(m_{\mathrm{h}},\ m_{\mathrm{A}})$ plane, and the interpolated signal and background likelihood histograms allow comparison of the data likelihood distribution with the signal and background predictions.

Signal events with $\mathrm{h}^0\mathrm{A}^0 \rightarrow \mathrm{b\bar{b}b\bar{b}}$ are easier to separate from the background than signal events with $\mathrm{h}^0\mathrm{A}^0 \rightarrow$ gggg since the gggg case has a poorer reconstructed mass resolution which deteriorates the $\log(\Delta\chi^2(m_{\mathrm{h}},\ m_{\mathrm{A}}))$ likelihood variable. The signal reference histograms are created using samples of $\mathrm{h}^0\mathrm{A}^0 \rightarrow \mathrm{b\bar{b}b\bar{b}}$ signal Monte Carlo events, and the signal likelihood histograms are filled with $\mathrm{h}^0\mathrm{A}^0 \rightarrow$ gggg events, ensuring the statistical independence of the reference and likelihood histograms, and also ensuring the conservativeness of the performance over the possible final states of the h^0 and A^0 decays.

Example likelihood distributions are shown in Figure 3 for all data collected in 1999 and 2000, along with the SM background expectations and signal expectations, for three test-mass hypotheses, $(m_{\mathrm{h}}, m_{\mathrm{A}}) =$ (50 GeV, 100 GeV), (50 GeV, 60 GeV), and (30 GeV, 60 GeV). The corresponding distributions of $\log(\Delta\chi^2(m_{\mathrm{h}},\ m_{\mathrm{A}}))$ are also shown to illustrate how the distributions of the signal, the expected backgrounds, and the candidates change with the test-mass hypothesis.

The distribution of the likelihood is used directly as the input to the limit calculation. In the presence of systematic uncertainties on the background rate, including bins with low expected signal-to-background ratios reduces the sensitivity of the search. A lower cut on the likelihood variable of 0.8 is chosen, independent of the test mass hypothesis, in order to improve the sensitivity of the search. Table 3 lists the numbers of events passing the likelihood cut for each of the test masses on the Monte Carlo grid, the expected backgrounds, and the expected signal efficiencies for the $\mathrm{h}^0\mathrm{A}^0 \rightarrow$ gggg decay hypothesis. The signal efficiencies are also calculated separately for the $\mathrm{c\bar{c}c\bar{c}}$, $\mathrm{b\bar{b}b\bar{b}}$, and the $\mathrm{b\bar{b}c\bar{c}}$ decay hypotheses. For nearly all test mass combinations, the $\mathrm{h}^0\mathrm{A}^0 \rightarrow$ gggg hypothesis yields the least efficiency, and for the remainder, the differences are within the uncertainties.

m_{h}	m_{A}	2f	4f	total	data	eff [%]	eff [%]	eff [%]	eff [%]
[GeV]	[GeV]	bkg	bkg	bkg		gggg	$\mathrm{c\bar{c}c\bar{c}}$	$\mathrm{b\bar{b}b\bar{b}}$	$\mathrm{b\bar{b}c\bar{c}}$
30.0	30.0	27.0	6.1	33.1±3.1	20	1.9±0.5	2.1	1.7	1.0
40.0	30.0	42.1	11.8	53.9±5.1	42	12.1±1.4	13.7	12.2	13.9
60.0	30.0	24.1	15.2	39.2±3.7	43	26.6±2.4	27.7	30.7	29.6
80.0	30.0	16.6	22.7	39.3±3.7	46	22.0±2.1	30.1	27.4	32.4
100.0	30.0	15.3	48.2	63.5±6.0	69	16.4±1.7	22.9	24.1	22.9
120.0	30.0	12.7	34.6	47.3±4.4	59	8.8±1.1	20.1	17.9	24.3
140.0	30.0	11.3	19.3	30.6±2.9	37	3.7±0.7	8.3	8.8	7.7
40.0	40.0	29.5	15.1	44.6±4.2	32	22.1±2.1	22.7	22.3	19.1
50.0	40.0	33.0	32.1	65.1±6.1	64	36.1±3.0	36.4	33.6	36.0
70.0	40.0	19.4	34.5	53.8±5.1	46	26.7±2.4	35.8	34.6	33.7
92.0	40.0	15.7	59.1	74.8±7.0	82	17.8±1.8	28.4	24.7	26.4
110.0	40.0	14.9	58.2	73.1±6.9	74	14.7±1.6	22.9	25.7	22.6
130.0	40.0	18.7	47.6	66.4±6.2	79	8.7±1.1	12.6	14.5	15.7
50.0	50.0	18.1	32.3	50.3±4.7	54	36.5±3.1	39.6	41.6	41.2
60.0	50.0	20.9	49.5	70.4±6.6	89	34.0±2.9	37.9	36.5	33.6
80.0	50.0	11.9	57.2	69.1±6.5	58	23.6±2.2	31.7	32.2	30.5
100.0	50.0	12.6	66.7	79.3±7.5	79	16.7±1.7	25.2	25.5	26.0
120.0	50.0	18.5	59.9	78.4±7.4	78	13.8±1.5	19.6	20.4	22.7
60.0	60.0	15.2	43.0	58.2±5.5	61	31.1±2.7	37.5	40.0	39.7
70.0	60.0	16.8	64.0	80.8±7.6	87	26.3±2.4	33.5	33.2	37.3
90.0	60.0	10.5	75.6	86.2±8.1	88	17.4±1.7	23.5	23.6	23.6
110.0	60.0	20.1	79.4	99.5±9.4	92	16.3±1.7	22.3	20.9	21.5
70.0	70.0	8.4	50.7	59.1±5.6	57	22.5±2.1	36.0	31.5	34.6
80.0	70.0	8.7	99.2	107.9±10.1	106	18.1±1.8	27.2	29.8	28.0
100.0	70.0	12.0	84.1	96.1±9.0	100	16.4±1.7	23.3	24.9	21.2
80.0	80.0	1.7	56.9	58.6±5.5	54	2.5±0.5	4.6	9.6	6.1
90.0	80.0	4.4	92.9	97.2±9.1	110	11.5±1.3	18.2	19.5	14.6
90.0	90.0	21.0	142.0	162.9±15.3	162	25.7±2.3	31.7	32.5	29.8

Table 3: The expected Standard Model backgrounds, observed data counts, and expected signal efficiencies for the flavour independent $\mathrm{h^0A^0}$ search as a function of the test mass hypotheses. All data collected in 1999 and 2000 are combined, and the signal efficiencies are luminosity-weighted averages. The efficiencies are listed separately for gggg, $\mathrm{c\bar{c}c\bar{c}}$, $\mathrm{b\bar{b}b\bar{b}}$ and $\mathrm{b\bar{b}c\bar{c}}$ decay hypotheses. The errors given in table are statistical and systematic added in quadrature.

3.3 Systematic Uncertainties

Because of the cut on the likelihood of 0.8, the systematic uncertainties are evaluated only for the numbers of events passing this likelihood cut. Correlations between the uncertainties on the signal and background rates, as well as between samples taken at different centre-of-mass energies are evaluated and used in the computation of the confidence levels.

- **Monte Carlo Statistics** For a typical point in the Monte Carlo test mass grid, the MC statistical error on the signal rate is 7 %, but it is larger for models for which both m_{h} and m_{A} are small, due to the lower signal efficiency for such models. For nearly all model points, the MC statistical uncertainty on the background rate is between 1.5 % and 3 %, but for signals when either m_{h} or m_{A} is low, it can be as large as 5 %. An overall uncertainty of 7 % and 3 % is taken for the signal and background rates, respectively.

- **Jet Energy Resolution** The jet energy resolution is uncertain in the barrel region by about 3–5 %, but this uncertainty is approximately 15 % in the endcap regions. Uncertain jet energy resolution results in approximately a 5 % uncertainty on both the signal and background rates.

- **Jet Energy Scale** The jet energy scale is uncertain at the 1 % level. The corresponding uncertainty on the rate of events passing the likelihood cuts is approximately 2 % for both the signal and the background.

- **Jet Angle Resolution** A 22 mrad angle resolution uncertainty in both θ and ϕ results in an uncertainty on the rate of events passing the likelihood cuts that is approximately 1 % for both the signal and the background.

- **Interpolation Uncertainty** To test the reliability of the interpolation procedure, a single Monte Carlo signal point on the grid is deleted, and the interpolation procedure is used to replace it, and the process is repeated for all MC grid points not on the edges. Using the differences found in the selection rates, an uncertainty of 3.5 % is assigned to the signal efficiency and an uncertainty of 4 % is assigned to the background rate due to interpolation errors.

- **Four-Fermion Cross-Section** Nearly all of the background at model points near the expected limit is from four-fermion production. It is dominated by $\mathrm{e^+e^-}\rightarrow\mathrm{W^+W^-}$ production, although $\mathrm{e^+e^-}\rightarrow\mathrm{Z^0Z^{0(*)}}$ contributes as well. A 2 % uncertainty is assessed on the production cross-section of these events [31].

- **Monte Carlo Background Sample Comparison** The `KK2F` Monte Carlo generator using `PYTHIA` as the fragmentation and hadronisation model was used to generate the central values for the $\mathrm{q\bar{q}}$ background rates. These rates were compared to the same `KK2F` sample but re-hadronised with `HERWIG`, and also with a sample generated entirely with `PYTHIA`. `KORALW` was used to generate the qqqq, the $\mathrm{q\bar{q}}\ell^+\ell^-$ and the $\mathrm{qq}\ell\nu_\ell$ background rate central values, and `grc4f` was used as the comparison generator. An uncertainty of 5.4 % is assessed on the background rates passing the likelihood cuts.

When all uncertainties are added in quadrature, the systematic error on the background rate is 9.4 % and the systematic error on the signal rate is typically 9.6 %, with larger values for the signal systematic uncertainty for models with low efficiency, due to the Monte Carlo statistical uncertainty. The correlations between the signal and background uncertainties and between years are taken into account. The Monte Carlo statistical error affects the signal and background predictions and are uncorrelated between energies, and signal and background. The other uncertainties are correlated between centre-of-mass energies.

4 Confidence level calculation

Following the statistical method described in [32, 33], the direct searches listed in Section 6.1 are combined to increase the Higgs boson discovery potential and, in case of absence of signal, the exclusion power.

The confidence levels are derived from a test statistic, Q, which is defined such that Q quantifies the compatibility of the data with two hypotheses: a) the background hypothesis, and b) the signal+background hypothesis. The confidence levels are computed from a comparison of the observed test statistic and its probability distributions for a large number of simulated experiments for these two hypotheses. The results of the different search channels are expressed in bins of discriminating variables defined in the individual searches (*e.g.* mass, likelihood, neural network output, etc.). The ratio $Q = \mathcal{L}_{\mathrm{s+b}}/\mathcal{L}_{\mathrm{b}}$ of the binned likelihoods for the two hypotheses is chosen as the test statistic. The confidence level for the background hypothesis, $\mathrm{CL_b}$, is defined as the probability to obtain values of Q no larger than the observed value Q_{obs}, given a large number of hypothetical experiments with background processes only, $\mathrm{CL_b} = \mathrm{P(Q \ \leq \ Q_{obs}|background)}$. Similarly, the confidence level for the signal+background hypothesis, $\mathrm{CL_{s+b}}$, is defined as the probability to obtain values of Q not larger than observed, given a large number of hypothetical experiments with signal and background processes, $\mathrm{CL_{s+b}} = P(Q \ \leq \ Q_{\mathrm{obs}}|\mathrm{signal+background})$. In principle, $\mathrm{CL_{s+b}}$ could be used to exclude the signal+background hypothesis, given a model for Higgs boson production. However, this procedure may lead to cases when a downward fluctuation of the background would allow hypotheses to be excluded for which the experiment has no sensitivity due to the small expected signal rate. Therefore the ratio $\mathrm{CL_s} = \mathrm{CL_{s+b}}/\mathrm{CL_b}$ is used. It is always greater than $\mathrm{CL_{s+b}}$ and the limit obtained in this way is thus conservative. We adopt this quantity for setting exclusion limits and consider a hypothesis to be excluded at the 95 % confidence level if the corresponding value of $\mathrm{CL_s}$ is less than 0.05.

The expected confidence levels are obtained by replacing the observed data with a large number of simulated events for the background only or signal+background hypotheses.

The effect of systematic uncertainties for the individual channels is calculated using a Monte Carlo technique. The signal and background estimations are varied within the bounds of the systematic uncertainties, assuming Gaussian distributions of the uncertainties. Correlations are taken into account. These variations are convoluted with the Poisson statistical variations of the assumed signal and background rates in the confidence level calculation. The effect of systematic uncertainties on the exclusion limits generally turns out to be small.

5 Model independent interpretation

Since no excess of data has been observed, the flavour independent search for $\mathrm{e^+e^-\to h^0A^0}$, described in Section 3, is used to set 95 % CL upper limits on the $\mathrm{h^0A^0}$ production cross-section assuming 100 % hadronic branching ratios. The cross–section for $\mathrm{e^+e^-\to h^0A^0}$ is determined by m_{h}, m_{A}, and the scale factor c^2, analogous to the $\cos^2(\beta-\alpha)$ factor of 2HDMs. The scale factor c^2 is defined as the ratio of the pair–production cross–section in the model considered and the pair–production cross–section given in Eq. (2) with $\cos^2(\beta-\alpha)=1$. The coupling limit is calculated by finding the value of c^2 for which $\mathrm{CL_s}=0.05$, assuming both the $\mathrm{h^0}$ and the $\mathrm{A^0}$ to decay 100 % hadronically. Figures 5 and 6 show the 95% median expected and observed upper limit on c^2, respectively, as a function of the test-mass hypotheses, (m_h, m_A).

The search for $\mathrm{e^+e^-\to h^0A^0\to}$hadrons is sensitive in the region where the production cross-section exceeds 200 fb for $\sqrt{s}$ between 189 GeV and 206 GeV. For 100% decays to hadrons and $c^2=1$, this corresponds to $m_\mathrm{h}+m_\mathrm{A}\sim 130$ GeV; for these test masses, the production cross-section does not change significantly between the centre-of-mass energies of the data used. Monte Carlo signal samples were generated with $m_\mathrm{h}+m_\mathrm{A}$ up to 170 GeV, but due to the low signal cross-sections for high mass Higgs bosons, the $1-\mathrm{CL_b}$ results are reported only up to $m_\mathrm{h}+m_\mathrm{A}=145$ GeV. The higher-mass Monte Carlo samples are needed to interpolate the reference and likelihood histograms over the entire range over which the results are produced.

The composition of the background which passes the likelihood cut depends strongly on the test-masses m_h and m_A. For low m_h and m_A, the 2f background dominates, but for models near the limit, the 4f background is the most important. The signal efficiency after the likelihood cut also depends strongly on the mass hypotheses. For $m_\mathrm{h}\sim m_\mathrm{A}\sim 30$ GeV, the 2f background is quite large and closely mimics the signal. Only a very small fraction of the signal and of the background passes the likelihood selection requirement because of the reduced separation power between the signal and the background – the signal efficiency for this particular model is only 1.9 ± 0.5%. This small efficiency is compensated by the large expected signal cross section for low Higgs masses. Another mass hypothesis where the signal efficiency is low is $m_\mathrm{h}\sim m_\mathrm{A}\sim 80$ GeV. In this case, the $\mathrm{W^+W^-}$ background is dominant, and the separation between the signal and the background is poor. For this model, the signal cross-section is between 70 fb at $\sqrt{s}=189$ GeV and 100 fb at $\sqrt{s}=206$ GeV and is therefore beyond the range of sensitivity of the search. Over much of the range of tested mass hypotheses, the signal efficiency is between 20% and 30%, and signal cross-sections as low as 200 fb are excluded.

To determine whether a signal was observed, we compute $1-\mathrm{CL_b}$ for each point in the (m_h, m_A) plane in the search region. Given the mass resolution of approximately 3 GeV for the sum of m_h and m_A, and approximately 7 GeV for the difference between m_h and m_A, there are approximately 160 independent searches each of which may have an excess or deficit, diluting the significance of $1-\mathrm{CL_b}$. Thus, more than one independent excess in $1-\mathrm{CL_b}$ is expected at the percent level. Figure 4 shows $1-\mathrm{CL_b}$ on a logarithmic scale as a function of m_h and m_A. Nowhere is $1-\mathrm{CL_b}$ below 1%.

As a result of the improved sensitivity of the analysis and the inclusion of data taken at higher centre-of-mass energies in the years 1999 and 2000, the excluded domains in Figure 6 are extended substantially beyond those obtained in [6].

6 Search channels and external constraints used in the 2HDM(II) interpretation

6.1 Data samples and final state topologies studied

The present study relies on the data collected by OPAL at $\sqrt{s} \approx m_{\mathrm{Z}}$ and from $\sqrt{s} \approx 183$ GeV to 209 GeV, the highest $\mathrm{e^+e^-}$ collision energy attained at LEP. This paper uses existing published analyses for all but the new $\mathrm{h^0A^0}$ flavour independent channel described in Section 3. Channels that use b-tagging provide useful information in regions of the 2HDM(II) parameter space where the Higgs bosons are expected to decay predominantly into $\mathrm{b\bar{b}}$ pairs. Flavour independent channels, not using any b-tagging information, are also included in the combination in order to explore the regions at low α or low $\tan\beta$, where the decays of the $\mathrm{h^0}$ and $\mathrm{A^0}$ bosons into $\mathrm{b\bar{b}}$ and $\tau^+\tau^-$pairs are suppressed. In Table 4 the references to the published OPAL papers for the direct search channels combined in the present 2HDM(II) interpretation are given, together with the corresponding centre-of-mass energies at which they were performed.

The channels used at $\sqrt{s} \approx m_{\mathrm{Z}}$, 183 and 189 GeV are the same as in [6]. The integrated luminosities, the numbers of candidate events, the expected SM backgrounds and the efficiencies for each of the b-tagging (flavour independent) $\mathrm{h^0Z^0}$ channels at $192 \leq \sqrt{s} \leq 209$ GeV are given in Table 5 (Table 6).

The detection efficiencies quoted in Tables 5 and 6 are given as examples for specific values of m_{h}.

The integrated luminosities, the numbers of candidate events, the expected SM backgrounds and the efficiencies for the most relevant b-tagged $\mathrm{h^0A^0}$ channels are given in Table 7.

When scanning the parameter space the efficiency is calculated for each point in the (m_{h}, m_{A}) plane for each of the final states considered.

6.2 External constraints

In addition to the combination of the direct search channels, the following external constraints are applied in every parameter space point considered:

(a) A powerful experimental constraint on extensions of the SM is the determination of the total width of the $\mathrm{Z^0}$ boson, Γ_{Z}, at LEP [37]. Any possible excess width obtained when subtracting the predicted SM width from the measured value of Γ_{Z}, $\Delta\Gamma_{\mathrm{Z}}$, can be used to place upper limits on the cross–section of $\mathrm{Z^0}$ decaying, as in the 2HDM, into final states with $\mathrm{h^0}$ and $\mathrm{A^0}$ bosons [38]. The maximum additional contribution to the total $\mathrm{Z^0}$ width that is compatible with the measured width at 95 % CL is $\Delta\Gamma_{\mathrm{Z}} = 6.5$ MeV, obtained from the latest LEP combined $\mathrm{Z^0}$ lineshape results [24]. An expected increase of the partial width of the $\mathrm{Z^0}$ is evaluated for each scanned parameter space point in the 2HDM(II); if it is found to exceed the experimental limit, the point is excluded.

(b) The decay mode independent search for $\mathrm{e^+e^-}\rightarrow\mathrm{SZ^0}$ [39], where S is any scalar particle produced in association with the $\mathrm{Z^0}$ boson, provides an upper limit on

	$\sqrt{s}$ **[GeV]**			
Decay topologies	m_{Z}	183	189	192 → 209
$\mathbf{h^0Z^0}$				
$\mathrm{b\bar{b}q\bar{q}}$, $\mathrm{b\bar{b}}\nu\bar{\nu}$, $\mathrm{b\bar{b}e^+e^-}$, $\mathrm{b\bar{b}}\mu^+\mu^-$, $\mathrm{b\bar{b}}\tau^+\tau^-$	NA	[6]	[6]	[14]
$\mathrm{q\bar{q}}\nu\bar{\nu}$, $\mathrm{q\bar{q}e^+e^-}$, $\mathrm{q\bar{q}}\mu^+\mu^-$, $\mathrm{q\bar{q}}\tau^+\tau^-$	[6]	NA	[6]	[34]
$\tau^+\tau^-\mathrm{q\bar{q}}$	[6]	[6]	[6]	[34]
$\mathrm{q\bar{q}q\bar{q}}$	NA	NA	[6]	[34]
$\mathbf{h^0A^0}$				
$\mathrm{q\bar{q}}\tau^+\tau^-$or $\tau^+\tau^-\mathrm{q\bar{q}}$	[6]	NA	NA	NA
$\mathrm{b\bar{b}b\bar{b}}$, $\mathrm{b\bar{b}}\tau^+\tau^-$or $\tau^+\tau^-\mathrm{b\bar{b}}$	NA	[6]	[6]	[35]
$\mathrm{q\bar{q}q\bar{q}}$	NA	NA	[6]	This paper
$\boldsymbol{m_{\mathrm{h}} \geq 2m_{\mathrm{A}}}$, $\mathbf{h^0A^0{\rightarrow}A^0A^0A^0}$				
$\mathrm{b\bar{b}b\bar{b}b\bar{b}}$	[6]	[6]	[6]	[35]
$\boldsymbol{m_{\mathrm{h}} \geq 2m_{\mathrm{A}}}$ **and** $\boldsymbol{m_{\mathrm{A}} \leq 2m_{\mathrm{b}}}$, $\mathbf{h^0Z^0{\rightarrow}A^0A^0Z^0}$				
$\mathrm{A^0{\rightarrow}c\bar{c}}$, $\tau^+\tau^-$, gg and $\mathrm{Z^0}{\rightarrow}\nu\bar{\nu}$, $\mu^+\mu^-$, $\mathrm{e^+e^-}$	NA	NA	[36]	[36]
$\boldsymbol{m_{\mathrm{h}} \geq 2m_{\mathrm{A}}}$, $\mathbf{h^0Z^0{\rightarrow}A^0A^0Z^0}$				
$\mathrm{b\bar{b}b\bar{b}q\bar{q}}$, $\mathrm{b\bar{b}b\bar{b}}\nu\bar{\nu}$	NA	[6]	[6]	[35]
$\mathrm{b\bar{b}b\bar{b}e^+e^-}$, $\mathrm{b\bar{b}b\bar{b}}\mu^+\mu^-$, $\mathrm{b\bar{b}b\bar{b}}\tau^+\tau^-$	NA	[6]	[6]	NA

Table 4: Direct search channels combined in the present interpretation of the 2HDM(II). The searches with $\mathrm{q\bar{q}}$ final states include gg production as well. The numbers in the table give the references to the OPAL publications where a full description of the channel can be found. Channels marked NA do not exist. The $\mathrm{h^0A^0{\rightarrow}q\bar{q}q\bar{q}}$ (gggg, $\mathrm{ggq\bar{q}}$) analysis for the data taken in the years 1999 and 2000 is new and is described in Section 3 of this paper.

the scaling factor k, defined as $\sigma_{\mathrm{SZ}} = k\sigma^{\mathrm{SM}}_{\mathrm{HZ}}$, where σ_{SZ} is the production cross-section for a scalar S in association with a $\mathrm{Z^0}$, and $\sigma^{\mathrm{SM}}_{\mathrm{HZ}}$ is the expected SM cross-section for $\mathrm{m_S} = m_{\mathrm{H_{SM}}}$. This translates into a limit on the production cross-section in each parameter space point of the 2HDM(II) for which $\sigma_{\mathrm{hZ}} > k\sigma^{\mathrm{SM}}_{\mathrm{HZ}}$ at 95 % CL.

(c) In regions of the 2HDM(II) parameter space for which $4 \leq m_{\mathrm{h}}$ $(m_{\mathrm{A}}) \leq 12$ GeV a special study was performed in [40], and 95 % CL limits were obtained on the Yukawa couplings of $\mathrm{h^0}$ and $\mathrm{A^0}$ to down-type fermions. These limits are applied as an external constraint in the scan of the the 2HDM(II) parameter space described in Section 7.

The production of any neutral low mass scalar particle in association with the $\mathrm{Z^0}$ was investigated in [41] and, for $m_{\mathrm{h}} \leq 9.5$ GeV, a mass-dependent upper limit on the Higgs boson production cross–section was obtained. This limit was translated in [6] into an upper limit on the production cross–section for m_{h} below 9.5 GeV, which was considered as an external constraint in combination with the $\mathrm{Z^0}$-width constraint

Channel $\mathrm{h^0Z^0}\rightarrow$	$\mathcal{L}$ [$\mathrm{pb^{-1}}$]	Data	Total bkg	eff [%]
$192 \leq \sqrt{s} \leq 202$ GeV				
$\mathrm{b\bar{b}q\bar{q}}$ (m_{h} = 100 GeV)	217.0	30	28.8 ± 4.2	42.0
$\mathrm{b\bar{b}}\nu\bar{\nu}$	212.7	10	13.9 ± 1.6	46.9
$\mathrm{b\bar{b}}\tau^+\tau^-/\tau^+\tau^-\mathrm{q\bar{q}}$	213.6	5	5.1 ± 0.8	25.8
$\mathrm{b\bar{b}e^+e^-}$	214.1	3	4.1 ± 0.7	57.2
$\mathrm{b\bar{b}}\mu^+\mu^-$	213.6	6	3.3 ± 0.5	62.5
$200 \leq \sqrt{s} \leq 209$ GeV				
$\mathrm{b\bar{b}q\bar{q}}$ (m_{h} = 115 GeV)	207.3	20	17.5 ± 2.6	40.0
$\mathrm{b\bar{b}}\nu\bar{\nu}$	207.2	11	8.9 ± 1.0	40.7
$\mathrm{b\bar{b}}\tau^+\tau^-/\tau^+\tau^-\mathrm{q\bar{q}}$	203.6	5	4.5 ± 0.7	25.6
$\mathrm{b\bar{b}e^+e^-}$	203.6	1	3.6 ± 0.7	52.9
$\mathrm{b\bar{b}}\mu^+\mu^-$	203.6	4	3.4 ± 0.5	59.2

Table 5: The $\mathrm{h^0Z^0}$ b-tagging channels for data collected in the year 1999 with $192 \leq \sqrt{s} \leq 202$ GeV, and for data collected in the year 2000 with $200 \leq \sqrt{s} \leq 209$ GeV, respectively. The integrated luminosities ($\mathcal{L}$), the numbers of events after the final likelihood or Neural Network cut for the data and the expected background, normalised to the data luminosity are shown. The errors on the total background include modeling uncertainties and Monte Carlo statistics. The last column shows the detection efficiencies for a Higgs boson with m_{h} = 100 GeV for the year 1999 data and m_{h} = 115 GeV for the year 2000. Since the four-jet channel relies on a mass-dependent analysis, the numbers quoted in the table are given as an example for m_{h}= 90 GeV (100) for the year 1999 (2000) data. For the four-jet channel, the efficiency is computed only for $\mathrm{h^0}\rightarrow \mathrm{b\bar{b}}$ decays, while for the missing-energy, electron and muon channels the efficiency is for all decays of the $\mathrm{h^0}$, assuming SM branching fractions. For the tau channel, the efficiency is quoted for the processes $\mathrm{Z^0h^0}\rightarrow\tau^+\tau^-(\mathrm{h^0}\rightarrow\mathrm{all})$ or $\mathrm{Z^0h^0}\rightarrow\mathrm{q\bar{q}}\tau^+\tau^-$ assuming SM branching fractions.

Channel $\mathrm{h^0Z^0}\rightarrow$	$\mathcal{L}$ [pb^{-1}]	Data	Total bkg.	eff [%]
192 $<$ $\sqrt{s}$ $<$ 202 GeV				
$\mathrm{q\bar{q}q\bar{q}}$ ($m_{\mathrm{h}} = 90$ GeV)	217.0	290	290.6 ± 37.7	52.0
$\mathrm{q\bar{q}}\nu\bar{\nu}$	212.7	68	70.8 ± 10.8	45.2
$\mathrm{q\bar{q}}\tau^+\tau^-/\tau^+\tau^-\mathrm{q\bar{q}}$	213.7	1	4.6 ± 0.8	27.1
$\mathrm{q\bar{q}e^+e^-}$	214.1	13	8.3 ± 2.5	58.6
$\mathrm{q\bar{q}}\mu^+\mu^-$	213.6	7	7.6 ± 1.5	64.8
200 $<$ $\sqrt{s}$ $<$ 209 GeV				
$\mathrm{q\bar{q}q\bar{q}}$ ($m_{\mathrm{h}} = 100$ GeV)	207.3	263	235.3 ± 28.2	55.0
$\mathrm{q\bar{q}}\nu\bar{\nu}$	208.2	55	62.3 ± 2.2	48.4
$\mathrm{q\bar{q}}\tau^+\tau^-/\tau^+\tau^-\mathrm{q\bar{q}}$	205.3	2	4.2 ± 0.8	21.0
$\mathrm{q\bar{q}e^+e^-}$	208.2	10	8.3 ± 2.5	58.8
$\mathrm{q\bar{q}}\mu^+\mu^-$	207.8	9	7.4 ± 1.4	62.4

Table 6: The $\mathrm{h^0Z^0}$ flavour independent channels for data collected in 1999 with $192 \leq \sqrt{s} \leq 202$ GeV and in year 2000 with $200 \leq \sqrt{s} \leq 209$ GeV: the integrated luminosities ($\mathcal{L}$), the numbers of events after the final likelihood or Neural Network cut for the data and the expected background, normalised to the data luminosity. The errors on the total background include modeling uncertainties and Monte Carlo statistical errors. The last column shows the detection efficiency for a Higgs boson decaying to quark or gluon pairs with $m_{\mathrm{h}} = 90$ GeV and with $m_{\mathrm{h}} = 100$ GeV for data collected in year 1999 and 2000, respectively. Since the four-jet channel relies on a mass-dependent analysis, the numbers quoted in the table are given as an example for $m_{\mathrm{h}} = 90$ GeV (100) for the year 1999 (2000) data.

Channel $\mathrm{h^0A^0}\rightarrow$	(m_{h}, m_{A}) [GeV]	$\mathcal{L}$ [pb^{-1}]	Data	Total bkg	eff [%]
192 $\leq$ $\sqrt{s}$ $\leq$ 209 GeV					
$\mathrm{b\bar{b}b\bar{b}}$	(90, 90)	424.3	22	19.9 ± 2.01	49.4
$\mathrm{b\bar{b}}\tau^+\tau^-$ / $\tau^+\tau^-\mathrm{b\bar{b}}$	(90, 90)	417.2	13	13.2 ± 2.02	42.5
$\mathrm{b\bar{b}b\bar{b}b\bar{b}}$	(100, 40)	424.3	22	19.9 ± 2.01	59.4
199 $\leq$ $\sqrt{s}$ $\leq$ 209 GeV					
$\mathrm{b\bar{b}b\bar{b}}\nu\bar{\nu}$	(100, 40)	207.2	19	17.2 ± 2.30	66.0
$\mathrm{b\bar{b}b\bar{b}q\bar{q}}$	(100, 40)	207.3	20	17.5 ± 2.6	31.5

Table 7: The $\mathrm{h^0A^0}$ channels for data collected in the years 1999 and 2000. The integrated luminosities ($\mathcal{L}$), the numbers of events after the final likelihood or Neural Network cut for the data and the expected background, normalised to the data luminosity. The errors on the total background include modeling uncertainties and Monte Carlo statistics. The last column shows the detection efficiency for the mass combination given in the first two columns.

(item (a) in the previous list). The decay mode independent results included as an external constraint (item (b) in the previous list) provide better exclusion power than the upper limit on Higgs boson production cross–section obtained in [41], increasing the exclusion power in the 2HDM(II) parameter space for low m_{h} values. The external constraint on the Yukawa couplings extends the exclusion power to regions of the 2HDM(II) parameter space with low values of m_{h} and m_{A} and large tanβ. In general, the external constraints applied in the present study improve significantly the results that were obtained in [6].

7 Two Higgs Doublet Model interpretations

The interpretation of the searches for the neutral Higgs bosons in the 2HDM(II) is done by scanning the parameter space of the model. Every (m_{h}, m_{A}, tanβ, α) point determines the production cross–section and the branching ratios to different final states. The 2HDM(II) parameter space covered by the present study is:

- $1 \leq m_{\mathrm{h}} \leq 130$ GeV, in steps of 1 GeV
- $3 \leq m_{\mathrm{A}} \leq 220$ GeV, in steps of 1 GeV;
  $300 \leq m_{\mathrm{A}} \leq 500$ GeV, in steps of 100 GeV;
  $0.5 \leq m_{\mathrm{A}} \leq 2.0$ TeV, in steps of 0.5 TeV
- $0.4 \leq \tan\beta \leq 40$, in steps of 1° in β, from $\beta = 22°$ to $\beta = 88°$ and an additional point corresponding to $\tan\beta = 40$
- $\alpha = -\pi/2, \ -\pi/4, \ 0, \ \pi/4$, and $\pi/2$

The values of α are chosen to extend the analysis to the particular cases of maximal and minimal mixing in the neutral CP-even sector of the 2HDM(II) ($\alpha = \pm\pi/4$ and $\pm\pi/2$, respectively) and of BR($\mathrm{h}^0 \rightarrow \mathrm{b\bar{b}}$) = 0 ($\alpha = 0$). The extreme cases $\alpha = \pm\pi/2$ are equivalent in the 2HDM(II) since the mass matrix of the CP-even neutral Higgs sector, containing the Higgs doublets, becomes diagonal. In [6] models with $1 \leq m_{\mathrm{h}} \leq 100$ GeV (in steps of 1 GeV), $5 \leq m_{\mathrm{A}} \leq 100$ GeV (in steps of 1 GeV, and larger steps up to 2 TeV), $0.4 \leq \tan\beta \leq 58$ (in steps of 1° in β) and $\alpha = -\pi/2, \ -3\pi/8, \ -\pi/4, \ -\pi/8$ and 0, were considered. The present study is extended to cover models with positive values of α ($\alpha = \pi/4$ and $\pi/2$), which are not allowed in the MSSM-like scenarios. Furthermore larger values of m_{h} and m_{A} are explored in this study, due to the increased sensitivity of the search channels to high m_{h} and m_{A} values: the data analysed have been collected at larger centre-of-mass energies and with larger luminosities than those in [6]. For $\tan\beta < 0.4$, the theoretical predictions become unreliable. For $\tan\beta > 40$ the width of the A^0 and h^0 becomes non-negligible. The decay mode independent study introduced in Section 6.2.[b] is providing exclusion from $m_{\mathrm{h}} \approx 1$ GeV down to 1 KeV, where the limit on the cross-section scaling factor, k, with respect to the Standard Model Higgs-strahlung cross-section is of the order of 0.06 [39]. Below $m_{\mathrm{A}} \approx 3$ GeV radiative corrections become unstable inducing large fluctuations in the calculated cross–sections.

In the present study the other two free parameters of the model, m_{H} and $m_{\mathrm{H}^{\pm}}$, are set at values of $m_{\mathrm{H}} = 210$ GeV and $m_{\mathrm{H}^{\pm}} = 1$ TeV, above the kinematically accessible region at LEP. A scan over values of the masses m_{H} and $m_{\mathrm{H}^{\pm}}$ up to 2 TeV has been performed and no change has been observed in the production cross–sections and branching ratios to final state topologies of h^0 and A^0, as expected from the theory. The `HZHA` Monte Carlo generator [16] that includes the 2HDM(II) production cross–sections and branching ratios of the Higgs particles has been used to scan the parameter space. This generator includes next-to-next-to-leading order QCD corrections and next-to-leading order electroweak corrections. The branching ratios and cross–sections obtained were cross–checked with the results of another generator [42] in which QCD corrections are computed only up to next-to-leading order. The comparison showed an agreement better than 1 % between the results of the two programs.

The results of all the individual search channels at the studied centre–of–mass energies are combined statistically to provide 95 % confidence level (CL) limits, which are extracted using the method explained in Section 4. By applying the external constraints discussed in Section 6.2 additional regions of the parameter space are excluded at 95 % CL. Although the flavour independent channels supply a unique way of investigating parameter space regions where the branching ratio $\mathrm{h}^0 \rightarrow \mathrm{b\bar{b}}$ or $\mathrm{A}^0 \rightarrow \mathrm{b\bar{b}}$ is highly suppressed (*e.g.*, low α and $\tan\beta$ regions), they have a poor sensitivity with respect to the b–tagging channels outside these regions. The use of b–tagging information substantially reduces the background coming from $\mathrm{W}^+\mathrm{W}^-$ events and improves the sensitivity of observing Higgs bosons even in regions of the 2HDM(II) parameter space where only small branching ratios for $\mathrm{h}^0 \rightarrow \mathrm{b\bar{b}}$ are expected. The flavour independent and b-tagging searches have candidate events in common, as is also true for the b-tag 4-jets $\mathrm{h}^0\mathrm{A}^0$ and $\mathrm{h}^0\mathrm{Z}^0$ searches. To avoid double–counting of candidate events, in each of the parameter space points only the channel that provides the better expected confidence level among the ones that have some candidates in common is used for the extraction of the limits.

The direct searches for the process $\mathrm{e}^+\mathrm{e}^- \rightarrow \mathrm{h}^0\mathrm{Z}^0$ ($\mathrm{e}^+\mathrm{e}^- \rightarrow \mathrm{h}^0\mathrm{A}^0$) in the Z^0 data contribute mainly in the $m_{\mathrm{h}} \leq 50$ GeV ($m_{\mathrm{h}} \leq 60$ GeV) region. For $\sqrt{s} \geq 189$ GeV, since the flavour independent $\mathrm{h}^0\mathrm{Z}^0$ and $\mathrm{h}^0\mathrm{A}^0$ analyses have been performed in the mass regions $m_{\mathrm{h}} \geq 60$ GeV and m_{h}, $m_{\mathrm{A}} \geq 30$ GeV, respectively, only b-tagging channels are applied below these masses. The flavour independent analyses provide exclusion for the whole $\tan\beta$ range and for the $\tan\beta < 1$ regions for $\alpha = 0$ and $\alpha = \pm\pi/4$, respectively.

In Figures 7(a–d) the excluded regions in the (m_{h}, m_{A}) plane are shown for the chosen values of α, together with the calculated expected exclusion limits. A particular (m_{h}, m_{A}, α) point is excluded at 95 % CL if it is excluded for all scanned values of $\tan\beta$. Different domains of $\tan\beta$ are studied and described below: a) $0.4 \leq \tan\beta \leq 40$ and b) $0.4 \leq \tan\beta \leq 1.0$ or $1.0 < \tan\beta \leq 40$, for which enlarged excluded regions are obtained.

a) $0.4 \leq \tan\beta \leq 40$ (darker grey area):

- For all α values, in the region below $m_{\mathrm{h}} \lesssim 10$ GeV the sensitivity of the channels at $\sqrt{s} \approx m_{\mathrm{Z}}$ is poor. The exclusion in this region is due to the application of the external constraints, as explained in section 6.2, in particular to the Z width constraint. Both the $\mathrm{h}^0\mathrm{Z}^0$ and $\mathrm{h}^0\mathrm{A}^0$ production processes contribute to the natural width of the Z^0. The exclusion provided by the $\mathrm{h}^0\mathrm{Z}^0$ process is valid for any value of m_{A}. On the other hand, the exclusion provided by the $\mathrm{h}^0\mathrm{A}^0$ process is kinematically limited to the regions where $m_{\mathrm{A}} + m_{\mathrm{h}} \leq m_{\mathrm{Z}}$. The contribution of the $\mathrm{h}^0\mathrm{Z}^0$ production cross–section to the Z^0 width depends on the argument $(\beta - \alpha)$, and it becomes large enough for this process alone to provide exclusion in different tanβ domains for the α values considered.

- The shape of the exclusion plot in Figures 7(a) and (b) for $m_{\mathrm{h}} < 30$ GeV is related to the kinematic constraint on the $\mathrm{h}^0\mathrm{A}^0$ production in the Z^0 data, which for $\beta - \alpha \approx 0$ or π is the only allowed process, since the $\mathrm{h}^0\mathrm{Z}^0$ production cross–section vanishes. Since the α values are such that the condition $\beta - \alpha \approx 0$ or π is never achieved in Figures 7(c) and (d), the domains with $m_{\mathrm{h}} + m_{\mathrm{A}} > \sqrt{s}$ can be excluded by the $\mathrm{h}^0\mathrm{Z}^0$ channels. For $m_{\mathrm{h}} >$ 20-30 GeV, the high energy data open a new kinematic region and are able to exclude large (m_{h}, m_{A}) areas, as can be seen in Figures 7(a) and (b). In the same figures the exclusion in the observed rectangular contour $20 \lesssim m_{\mathrm{h}} \lesssim 30$ GeV and $90 \lesssim m_{\mathrm{A}} \lesssim 110$ GeV is due to the recent optimisation of the $\mathrm{e}^+\mathrm{e}^- \to \mathrm{h}^0\mathrm{A}^0 \to \mathrm{b\bar{b}b\bar{b}}$ analysis in the same kinematical region [35]. The unexcluded region $20 \lesssim m_{\mathrm{h}} \lesssim 30$ GeV and $60 \lesssim m_{\mathrm{A}} \lesssim 90$ GeV is due to a small excess in the data with respect to the expected background of about the same size as the expected signal, for tan$\beta \approx 8$ in Figure 7(a) and for tan$\beta \approx 0.7$ in Figure 7(b), respectively.

- The (m_{h}, m_{A}) points below the semi-diagonal defined by $m_{\mathrm{h}} \geq 2m_{\mathrm{A}}$, for which the process $\mathrm{h}^0 \to \mathrm{A}^0\mathrm{A}^0$ is kinematically allowed, can only be excluded by the high energy channels for restricted tanβ ranges depending on the α values examined. For very low values of tanβ the branching ratio for $\mathrm{A}^0 \to \mathrm{b\bar{b}}$ vanishes, causing unexcluded regions for all values of α. However, these are excluded by the Z^0 data flavour independent analyses below $m_{\mathrm{h}} \approx 60$ GeV. The region for $m_{\mathrm{A}} \leq 10$ GeV is difficult to exclude since the decay $\mathrm{h}^0 \to \mathrm{A}^0\mathrm{A}^0$ is usually dominant when kinematically allowed and the A^0 cannot decay to $\mathrm{b\bar{b}}$. Therefore the searches using b-tagging do not help in this region, while the sensitivity of the flavour independent $\mathrm{h}^0\mathrm{Z}^0$ channels is too low to provide any exclusion. For $\alpha = 0$ and $\alpha = -\pi/4$, the exclusion in this region is obtained by using the dedicated search for the process $\mathrm{h}^0\mathrm{Z}^0 \to \mathrm{A}^0\mathrm{A}^0\mathrm{Z}^0$ followed by $\mathrm{A}^0 \to \mathrm{c\bar{c}}$, $\tau^+\tau^-$, gg and $\mathrm{Z}^0 \to \nu\bar{\nu}$, $\mu^+\mu^-$, $\mathrm{e}^+\mathrm{e}^-$. By applying the Yukawa external constraint large tanβ values are excluded.

- The region $55 \leq m_{\mathrm{h}} \leq 60$ GeV and $m_{\mathrm{A}} \geq 75$ GeV for $\alpha = 0$ in Figure 7(c) is not excluded for tan$\beta \leq 1$ since for the Z^0 data the $\mathrm{h}^0\mathrm{Z}^0$ cross-section becomes too small to exclude it and most of the high energy flavour independent channels are only efficient for domains in which $m_{\mathrm{h}} \geq 60$ GeV.

- The largest (m_{h}, m_{A}) excluded domain is for $\alpha = -\pi/4$, where most of the parameter space points accessible at LEP are excluded, as can be seen in Figure 7(d).

b) $0.4 \leq$ tan$\beta \leq 1.0$ (lighter grey area) and $1.0 <$ tan$\beta \leq 40$ (hatched area):

- In Figure 7(c), as a consequence of the variation of the $\mathrm{h}^0\mathrm{Z}^0$ production cross–section with tanβ, as discussed above, the $m_{\mathrm{h}} < 10$ GeV and $55 \leq$

$m_{\rm h} \leq 60$ GeV, $m_{\rm A} \geq 75$ GeV regions are excluded for all values of $m_{\rm A}$ in the tan$\beta > 1.0$ domain. For $\alpha = \pm\pi/2$ the $m_{\rm h} < 30$ GeV region is excluded for all values of $m_{\rm A}$ only in the tan$\beta \leq 1.0$ domain. In the same figure, the region $m_{\rm h} \sim 90$ GeV and $m_{\rm A} \geq 60$ GeV has an excess of data in the four-jet flavour independent $\rm h^0Z^0$ channel at 90 GeV and therefore cannot be excluded even for tan$\beta \geq 1$.

- At $\alpha = 0$ and small values of tanβ the production cross–section for the process $\rm e^+e^- \to h^0Z^0$ is highly suppressed. For $m_{\rm h} > 60$ GeV, constraining tan$\beta > 1.0$, larger excluded regions are obtained, as can be seen in Figure 7(c) (hatched area). In the same figure, the unexcluded domain $88 \lesssim m_{\rm h} \lesssim 92$ GeV, $m_{\rm A} > 60$ GeV for tan$\beta > 1$ is due to the presence of candidates in the flavour independent four-jet channel in the year 2000 data [34].
- For $\alpha = \pm\pi/2$, Figure 7(a), the region $100 \lesssim m_{\rm h} \lesssim 110$ GeV and $35 \lesssim m_{\rm A} \lesssim 50$ GeV is unexcluded due to the presence of candidate events in the $\rm h^0A^0 \to b\bar{b}b\bar{b}$ and $\rm h^0A^0 \to b\bar{b}\tau^+\tau^-$ channels in the high energy data [35].

In Figure 8 the excluded regions in the ($m_{\rm h}$, $m_{\rm A}$) plane independent of α are given together with the expected exclusion limits from MC studies. A particular ($m_{\rm h}$, $m_{\rm A}$) point is excluded at 95 % CL if it is excluded for all scanned values of tanβ and α. Different domains of tanβ are shown: $0.4 \leq$ tan$\beta \leq 40$ (darker grey area), $0.4 \leq$ tan$\beta \leq 1.0$ (lighter grey area) and $1.0 <$ tan$\beta \leq 40$ (hatched area), for which enlarged excluded regions are obtained. A rectangular region $1 \lesssim m_{\rm h} \lesssim 55$ GeV for $3 \lesssim m_{\rm A} \lesssim 63$ GeV is fully excluded at 95 % CL independent of α and tanβ. The scanned $\alpha > 0$ domain is new with respect to [6] and has the effect of restricting the exclusion for tan$\beta \leq 1$ to the kinematically accessible region for the $\rm h^0A^0$ production.

For completeness, the excluded regions in the ($m_{\rm h}$, $m_{\rm A}$) plane for $\alpha \leq 0$ are given together with the calculated expected exclusion limits, is shown in Figure 9. The present study considerably extends the excluded ($m_{\rm h}$, $m_{\rm A}$) domain for negative values of α when compared with the study published in [6]. The previously excluded region of $1 \lesssim m_{\rm h} \lesssim 44$ GeV and $12 \lesssim m_{\rm A} \lesssim 56$ GeV is now enlarged to $1 \lesssim m_{\rm h} \lesssim 55$ GeV and $3 \lesssim m_{\rm A} \lesssim 63$ GeV, for all tanβ values for negative α.

In Figures 10(a–d) the excluded regions in the (tanβ, $m_{\rm h}$) plane are shown for the chosen values of α, together with the calculated expected exclusion limits. A particular ($m_{\rm h}$, tanβ, α) point is excluded at 95 % CL if it is excluded for all scanned values of $m_{\rm A}$. There are two regions shown, the whole domain 3 GeV $\leq m_{\rm A} \leq$2 TeV (darker grey area) and a restricted domain for which $3 \leq m_{\rm A} \leq 60$ GeV (lighter grey area). The exclusion contours for $m_{\rm A} \leq 60$ GeV are larger for all α values, and entirely contain the 3 GeV $\leq m_{\rm A} \leq$ 2 TeV excluded areas.

Note that in Figure 10(b) the region tan$\beta \approx 1$ is unexcluded due to the suppression of the $\rm h^0Z^0$ production cross–section as $\beta - \alpha \approx 0$, while relatively low values of tanβ can be excluded for $1 \leq m_{\rm h} \leq 60$ GeV (darker grey area). Restricting the values of $m_{\rm A}$ to be lower than 60 GeV improves the exclusion since the kinematical limit for $\rm h^0A^0$ production mechanism is never reached.

In Figure 11 the excluded regions in the ($m_{\rm A}$, tanβ) plane are shown for different values of α, together with the expected exclusion limits. A particular ($m_{\rm A}$, tanβ, α) point is excluded at 95 % CL if it is excluded for all scanned values of $m_{\rm h}$. There are three regions shown, corresponding to different m_{h} domains that are subsets of one another, namely: $1 \leq m_{\mathrm{h}} \leq 110$ GeV (darker grey area), $1 \leq m_{\mathrm{h}} \leq 90$ GeV (lighter grey area) and $1 \leq m_{\mathrm{h}} \leq 75$ GeV (hatched area). The lower the m_{h} upper value analysed, the larger the excluded (m_{A}, tanβ) region.

In Figures 11 (a), (b) and (c) for $m_{\mathrm{A}} < 10$ GeV and tan$\beta > 10$ the excluded domains are a direct application of the Yukawa external constraint.

Figures 11 (a) and (b) and Figures 10 (a) and (b) show a similar behaviour in the tanβ excluded domains: for $\alpha = \pm\pi/2$ ($\alpha = \pi/4$) mostly low (large) tanβ values are excluded.

In Figure 11 (c) for $1 \leq m_{\mathrm{h}} \leq 90$ GeV the area with $m_{\mathrm{A}} > 45$ GeV and tan$\beta > 1$ is excluded as expected from the tan$\beta > 1$ contour in Figure 7 (c). In Figure 11 (d) the unexcluded region in the dark grey contour for small tanβ and $m_{\mathrm{A}} < 50$ GeV corresponds to the unexcluded region under the semidiagonal in Figure 7 (d). As can be seen in Figure 11 (d) for $1 \leq m_{\mathrm{h}} \leq 90$ GeV, the area $24 < m_{\mathrm{A}} < 32$ GeV for $3 <$ tan$\beta < 14$ is not excluded, but it is excluded when $1 \leq m_{\mathrm{h}} \leq 75$ GeV as inferred from Figure 7 (d).

In Figures 11 (b) and (d) for $1 \leq m_{\mathrm{h}} \leq 110$ GeV the area $10 < m_{\mathrm{A}} < 25$ GeV for tan$\beta > 20$ is excluded thanks to the optimisation of the $\mathrm{e^+e^-\to h^0A^0 \to b\bar{b}b\bar{b}}$ analysis in the same kinematical region [35].

8 Conclusions

New limits on the $\mathrm{h^0A^0}$ pair-production cross-section are obtained by the application of a new flavour independent $\mathrm{h^0A^0}$ analysis at the highest LEP energies. A lower bound at 95 % CL is extracted along the diagonal at $m_{\mathrm{h}} \approx m_{\mathrm{A}} \approx 71$ GeV for $c^2 = 1$ assuming 100 % hadronic decays. The limit obtained by using the b-tagging analysis [35] and assuming 100 % decays into b-quarks, is at $m_{\mathrm{h}} \approx m_{\mathrm{A}} \approx 81$ GeV for $c^2 = 1$.

A general analysis of the 2HDM(II) with no CP violation and no extra particles besides those of the SM and the five Higgs bosons has been performed using the $\mathrm{Z^0}$, 183 and 189 GeV data together with the high energy data taken by OPAL in the years 1999 and 2000 at $\sqrt{s} = 192 - 209$ GeV. Large areas of the parameter space of the model have been scanned. In the scanning procedure the dependence of the production cross–sections and branching ratios on the angles α and β, calculated with next-to-next-to-leading order QCD corrections and next-to-leading order electroweak corrections, has been considered.

In addition to the standard OPAL b–tagging analyses, flavour independent channels for both the Higgs-strahlung process, $\mathrm{e^+e^-\to h^0Z^0}$, and the pair–production process, $\mathrm{e^+e^-\to h^0A^0}$, have been analysed, providing access to regions of parameter space in the 2HDM(II) where $\mathrm{h^0}$ and $\mathrm{A^0}$ are expected to decay predominantly into up–type light quarks and gluons (*e.g.* $\alpha \approx 0$).

The 2HDM(II) parameter space scan, for $1 \leq m_{\mathrm{h}} \leq 130$ GeV, 3 GeV $\leq m_{\mathrm{A}} \leq$ 2 TeV, $-\pi/2 \leq \alpha \leq \pi/2$ and $0.4 \leq$ tan$\beta \leq 40$, leads to large regions being excluded at the 95 % CL in the (m_{h}, m_{A}) plane as well as in the (m_{h}, tanβ) and (m_{A}, tanβ) projections. The region $1 \lesssim m_{\mathrm{h}} \lesssim$ 55 GeV and $3 \lesssim m_{\mathrm{A}} \lesssim 63$ GeV is excluded at 95 % CL both when restricting $\alpha \leq 0$, as in a MSSM-like scenario, and in the general 2HDM(II) case, independently of α within the scanned parameter space.

The results obtained by adding the data taken by OPAL in the years 1999 and 2000 substantially enlarge the excluded domains in the 2HDM(II) parameter space accessible by LEP.

Acknowledgements

We particularly wish to thank the SL Division for the efficient operation of the LEP accelerator at all energies and for their close cooperation with our experimental group. In addition to the support staff at our own institutions we are pleased to acknowledge the
Department of Energy, USA,
National Science Foundation, USA,
Particle Physics and Astronomy Research Council, UK,
Natural Sciences and Engineering Research Council, Canada,
Israel Science Foundation, administered by the Israel Academy of Science and Humanities,
Benoziyo Center for High Energy Physics,
Japanese Ministry of Education, Culture, Sports, Science and Technology (MEXT) and a grant under the MEXT International Science Research Program,
Japanese Society for the Promotion of Science (JSPS),
German Israeli Bi-national Science Foundation (GIF),
Bundesministerium für Bildung und Forschung, Germany,
National Research Council of Canada,
Hungarian Foundation for Scientific Research, OTKA T-038240, and T-042864,
The NWO/NATO Fund for Scientific Research, the Netherlands.

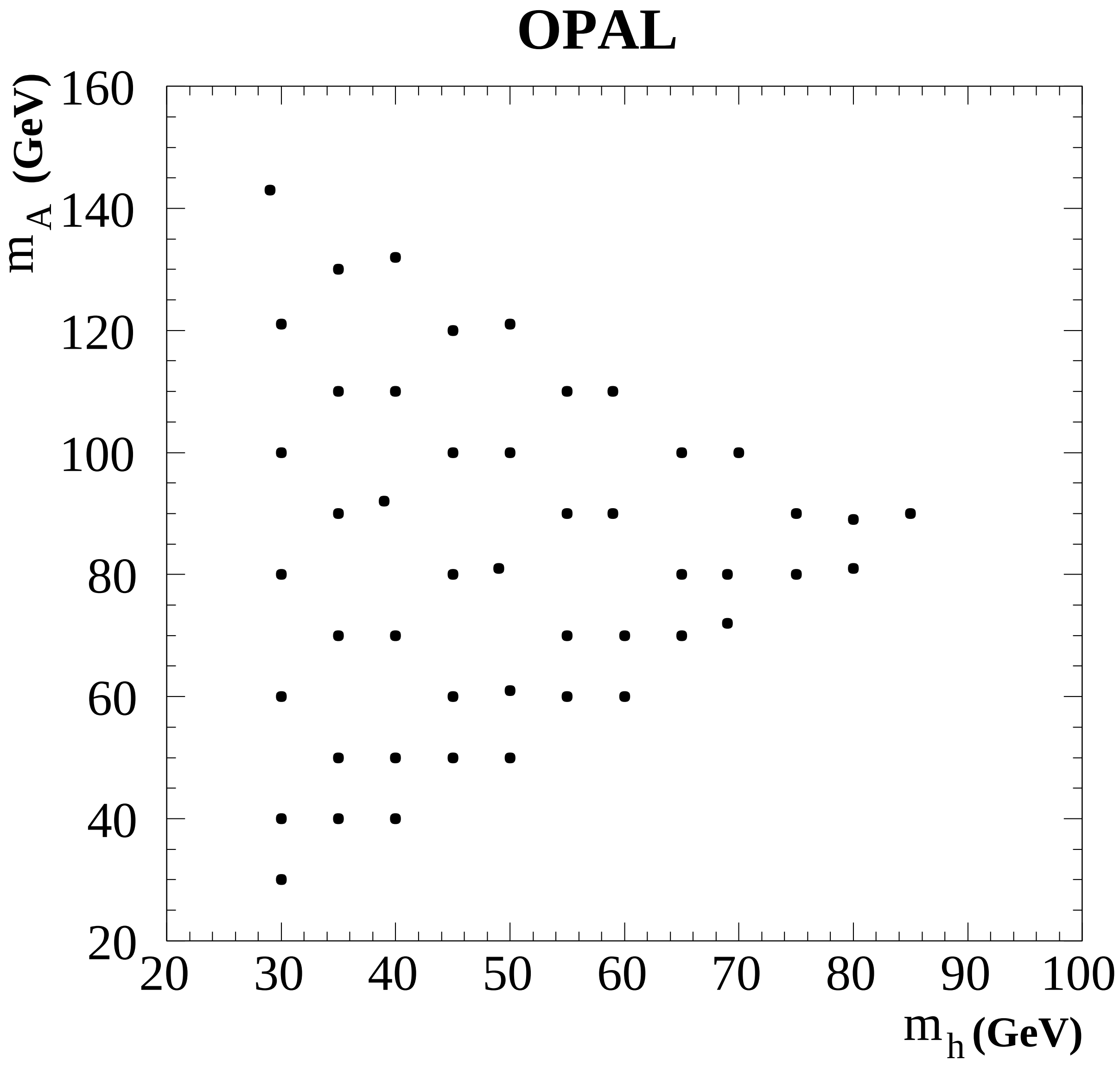

Figure 1: The Monte Carlo mass grid on which the signal was generated for the year 2000 analysis. Similar grids are used for the four 1999 samples.

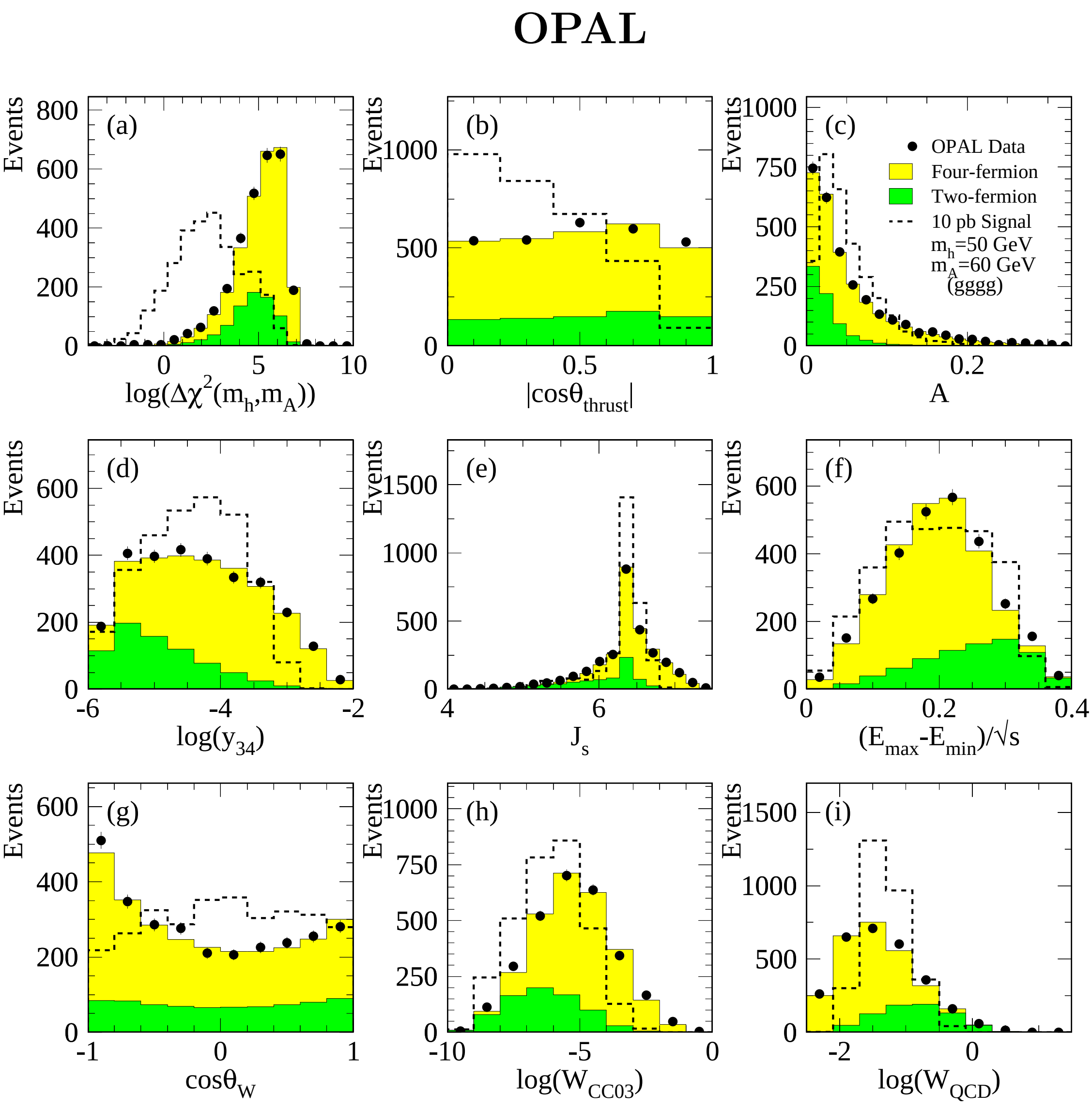

Figure 2: Distributions of the likelihood input variables for preselected events in the flavour-independent hadronic $\mathrm{h}^0\mathrm{A}^0$ search: (a) $\log(\Delta\chi^2(m_{\mathrm{h}}, m_{\mathrm{A}}))$, (b) $|\cos\theta_{\mathrm{thrust}}|$, (c) the event aplanarity A, (d) $\log(y_{34})$, (e) J_s, (f) $(E_{\mathrm{max}} - E_{\mathrm{min}})/\sqrt{s}$, (g) the jet-charge-signed $\cos\theta_{\mathrm{W}}$, (h) $\log(\mathrm{W}_{\mathrm{CC03}})$, and (i) $\log(\mathrm{W}_{\mathrm{QCD}})$. The dark-shaded histograms show the two-fermion ($\mathrm{q}\bar{\mathrm{q}}$) background, the light-shaded histograms show the four-fermion background. The backgrounds are shown stacked atop one another. The dashed histograms show a 10 pb signal of $\mathrm{e}^+\mathrm{e}^- \to \mathrm{h}^0\mathrm{A}^0 \to$ gggg with $m_{\mathrm{h}} = 50$ GeV and $m_{\mathrm{A}} = 60$ GeV, and the points with error bars show the OPAL data collected in 1999 and 2000.

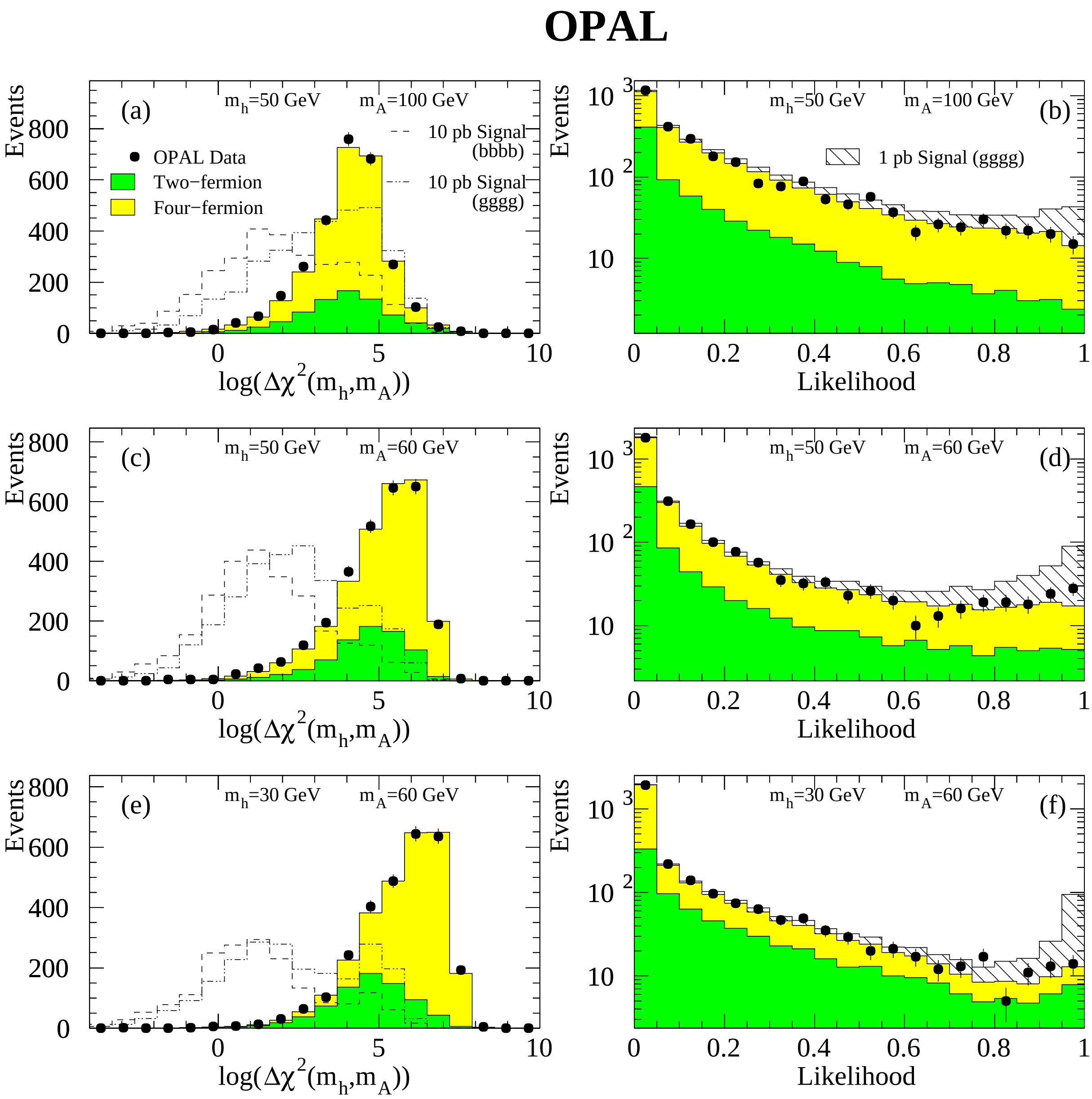

Figure 3: Distributions of the $\log(\Delta\chi^2(m_\mathrm{h}, m_\mathrm{A}))$ variable and the likelihood output variable for three test-mass hypotheses, $(m_\mathrm{h},\ m_\mathrm{A})$=(50 GeV, 100 GeV), (50 GeV, 60 GeV), and (30 GeV, 60 GeV). OPAL data are shown with the points, light-shaded histograms show the four-fermion Standard Model background expectations, and dark-shaded histograms show the two-fermion ($\mathrm{q\bar{q}}$) Standard Model background expectations. The two background rates are shown stacked in all histograms. In the likelihood histograms, a 1 pb signal assumed to decay to gggg is shown with the hatched histograms, added on top of the background sum. For the $\log(\Delta\chi^2(m_\mathrm{h}, m_\mathrm{A}))$ distributions, a 10 pb signal assumed to decay to $\mathrm{b\bar{b}b\bar{b}}$ is shown with dot-dashed histograms which are not added to the background, while a 10 pb signal assumed to decay to gggg is shown with dotted histograms, also not added to the background.

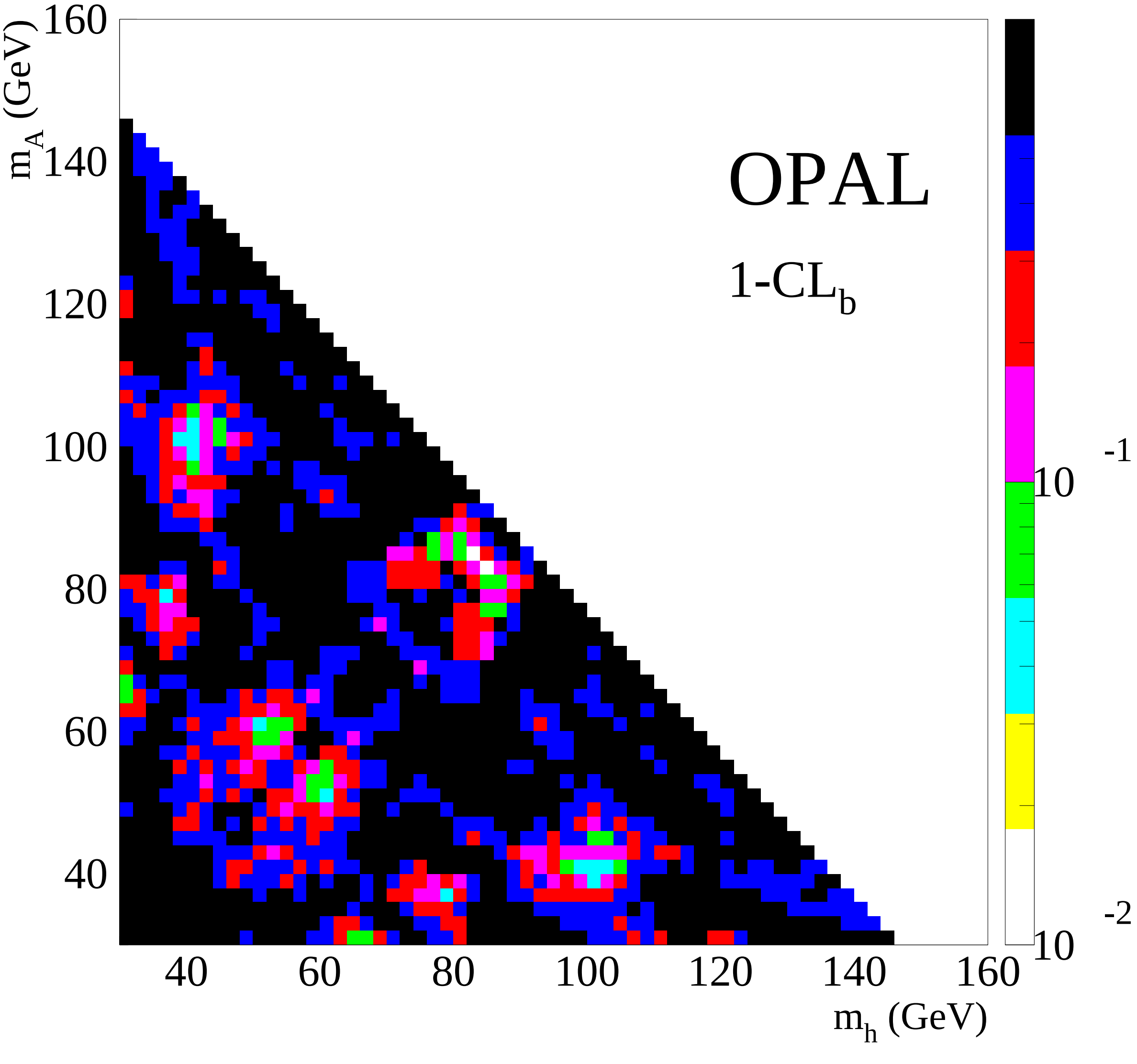

Figure 4: The value of $1 - \mathrm{CL_b}$ as a function of $(m_\mathrm{h}, m_\mathrm{A})$. No model has $1 - \mathrm{CL_b} < 0.01$, and one or more excesses with significance $1 - \mathrm{CL_b} < 0.01$ are expected due to the large number of independent searches conducted.

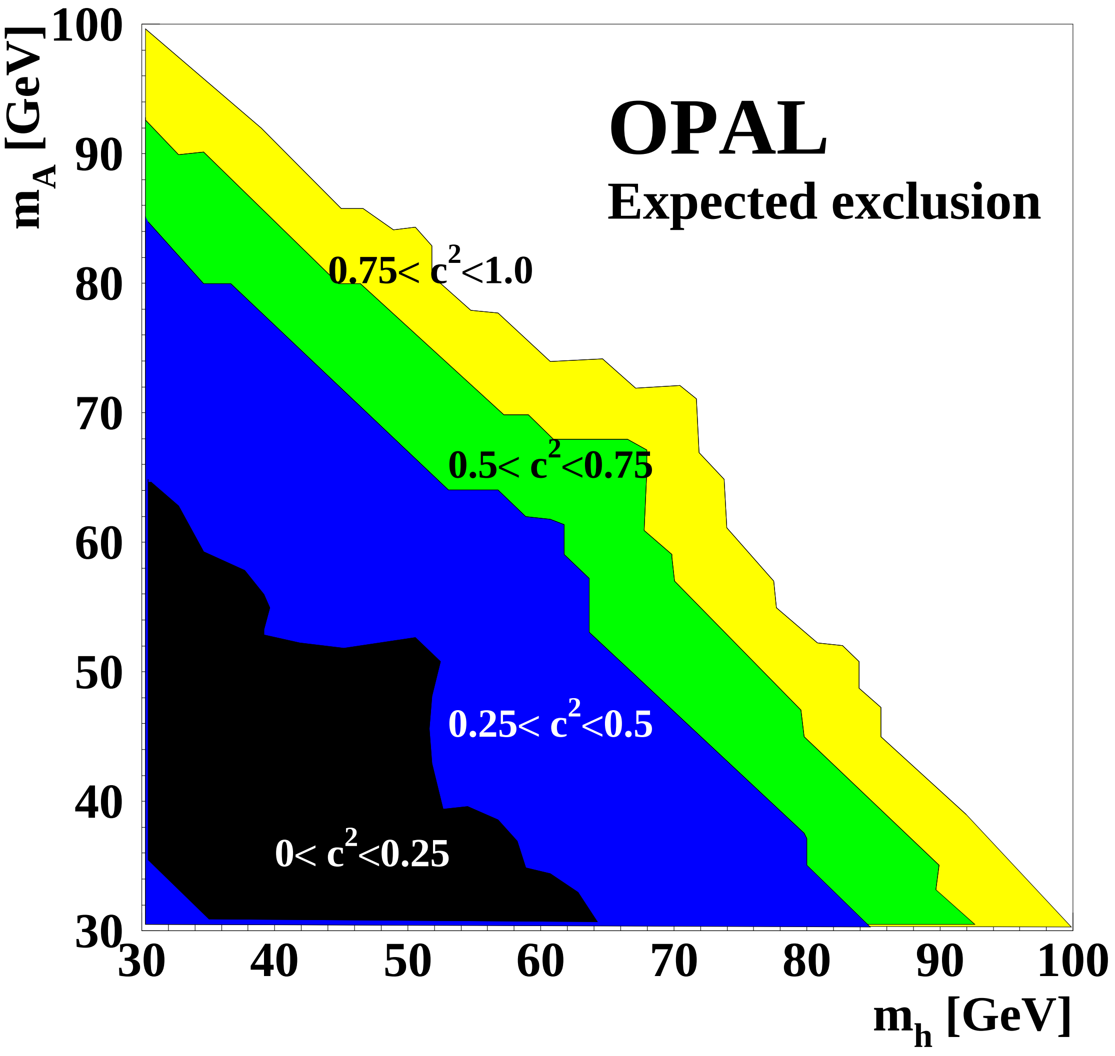

Figure 5: The median expected limit on the coupling c^2. Both the h^0 and the A^0 are assumed to decay hadronically 100% of the time.

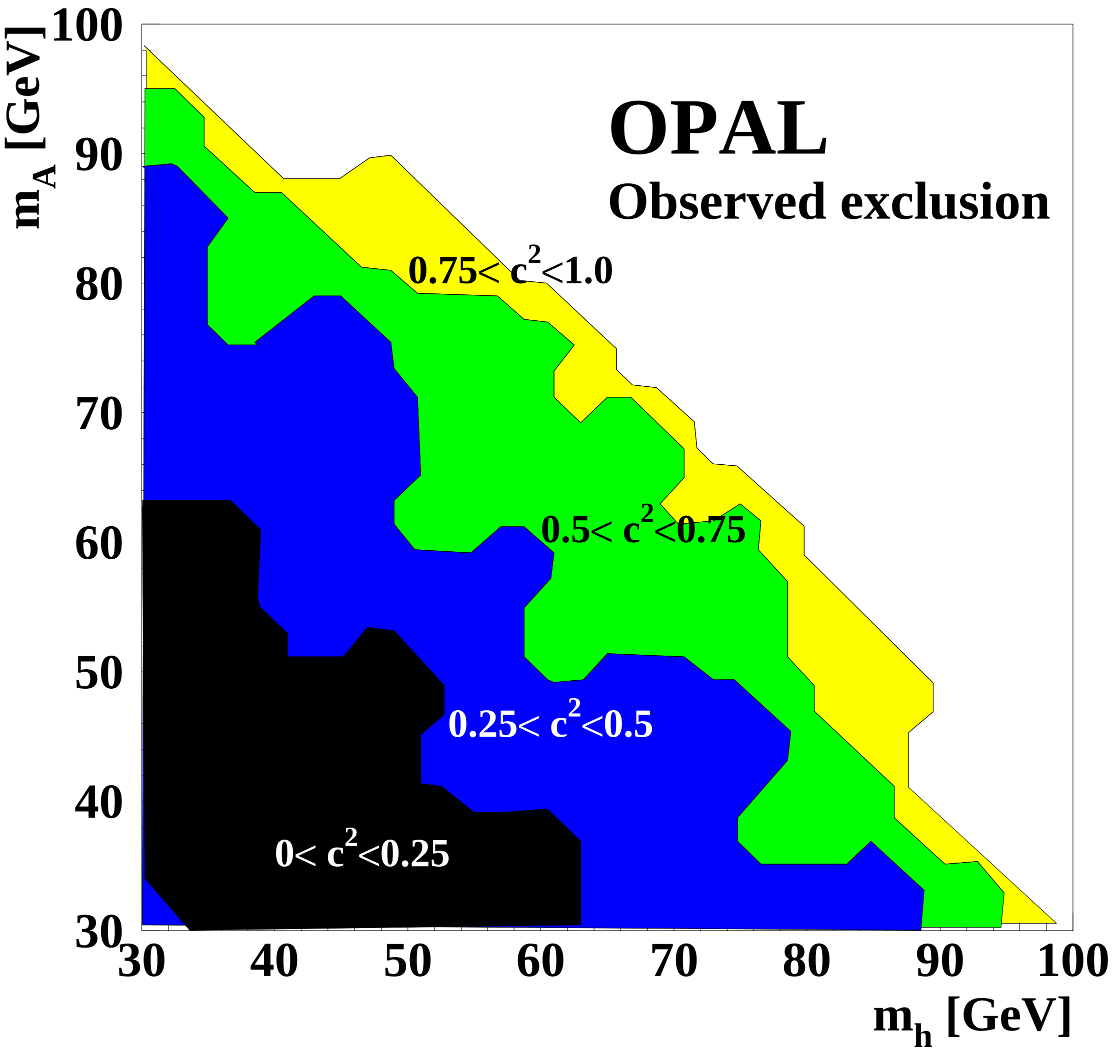

Figure 6: The limit on the coupling c^2. Both the h^0 and the A^0 are assumed to decay hadronically 100% of the time.

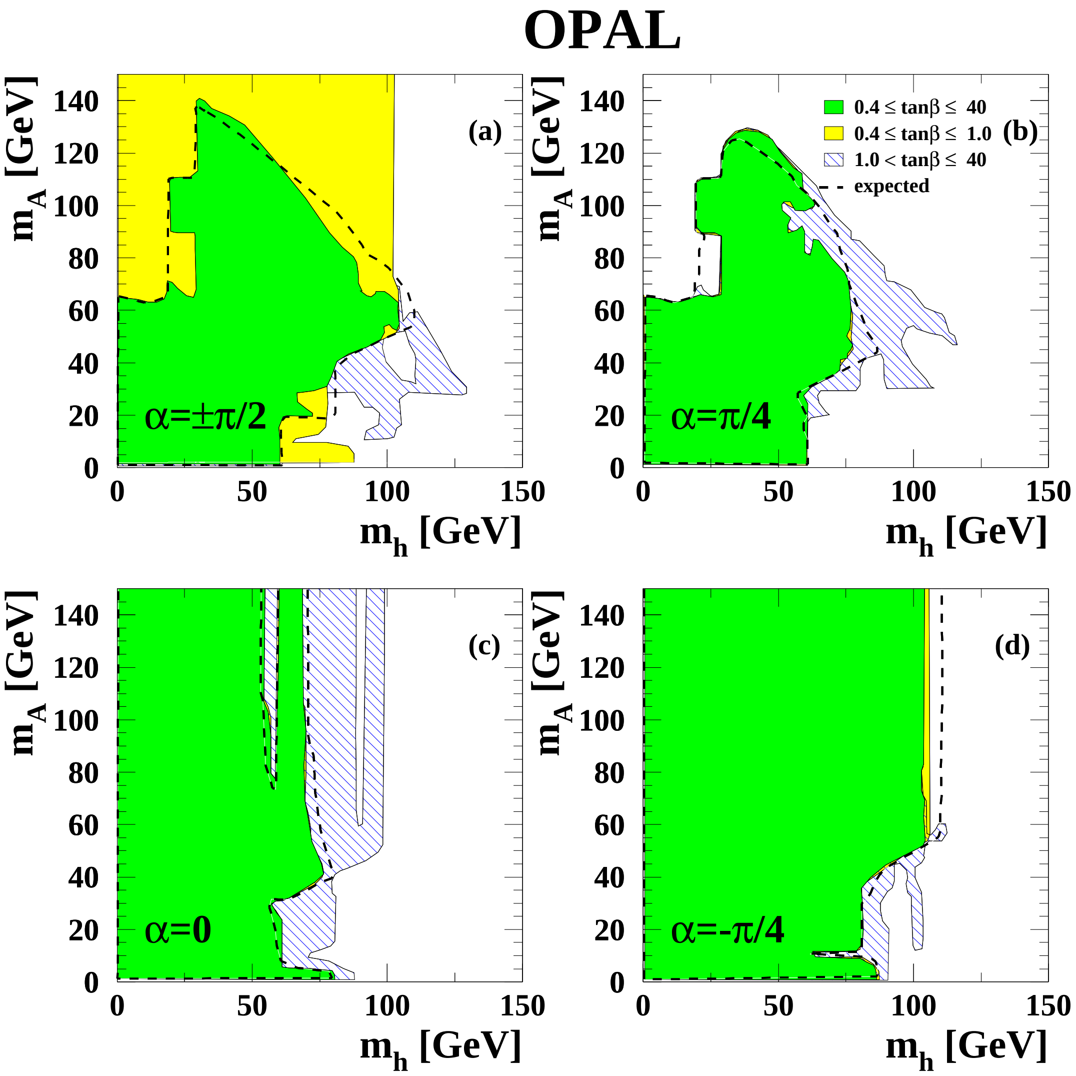

Figure 7: Excluded regions in the (m_{h}, m_{A}) plane, (a)–(d), for $\alpha = \pm\pi/2$, $\pi/4$, 0 and $-\pi/4$, respectively, together with the expected exclusion limits. A particular (m_{h}, m_{A}, α) point is excluded at 95% CL if it is excluded for all scanned values of tanβ. Three different domains of tanβ are shown: the darker grey region is excluded for all values $0.4 \leq$ tan$\beta \leq 40$; additional enlarged excluded regions are obtained constraining $0.4 \leq$ tan$\beta \leq 1.0$ (lighter grey area) or $1.0 <$ tan$\beta \leq 40$ (hatched area). Expected exclusion limits for $0.4 \leq$ tan$\beta \leq 40$ are shown as a dashed line.

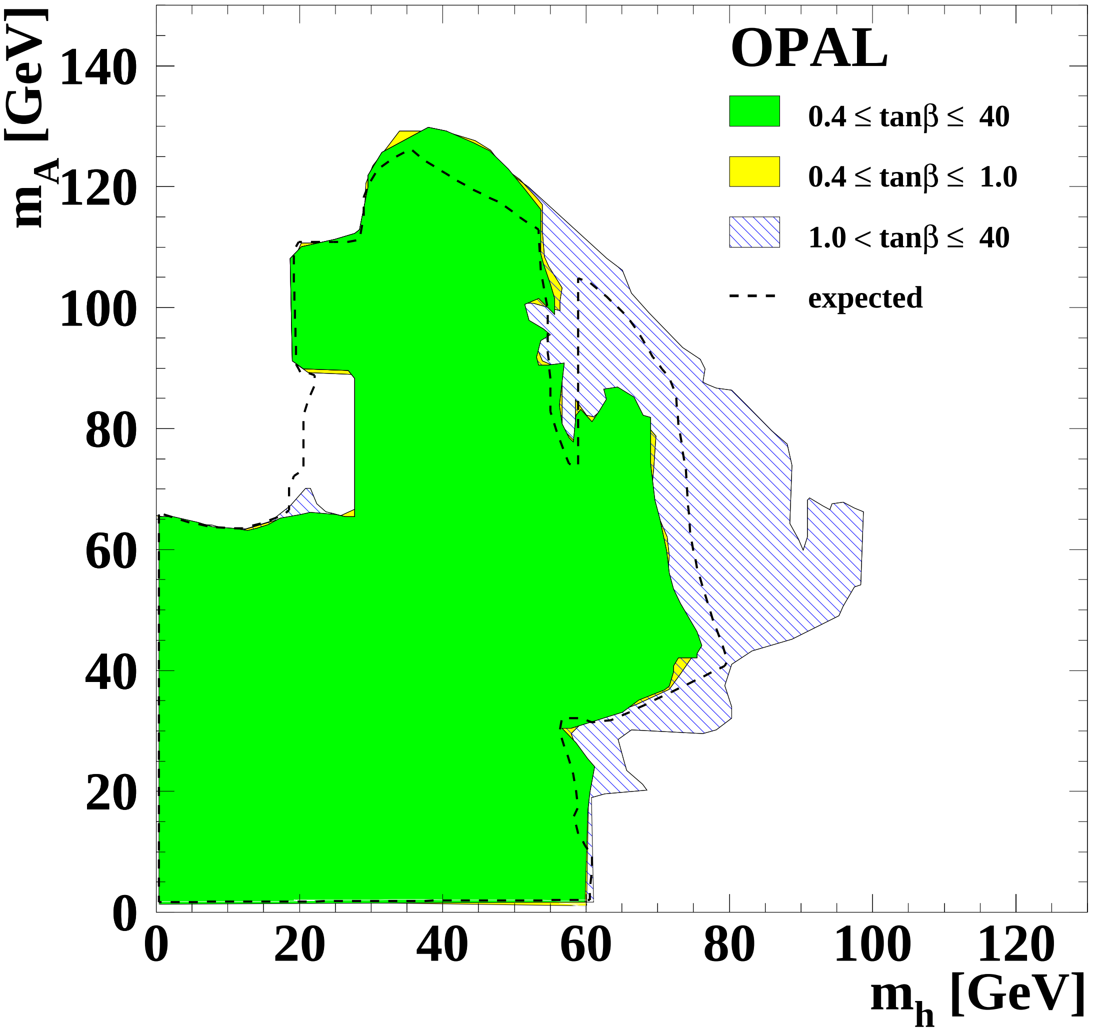

Figure 8: Excluded ($m_{\rm A}$, $m_{\rm h}$) region independent of α, together with the expected exclusion limit. A particular ($m_{\rm A}$, $m_{\rm h}$) point is excluded at 95% CL if it is excluded for 0.4 $\leq$ tanβ $\leq$ 40 (darker grey region), 0.4 $\leq$ tanβ $\leq$ 1.0 (lighter grey region) and 1.0 $<$ tanβ $\leq$ 40 (hatched region) for any α. Expected exclusion limits for 0.4 $\leq$ tan$\beta$$\leq$ 40 are shown as a dashed line.

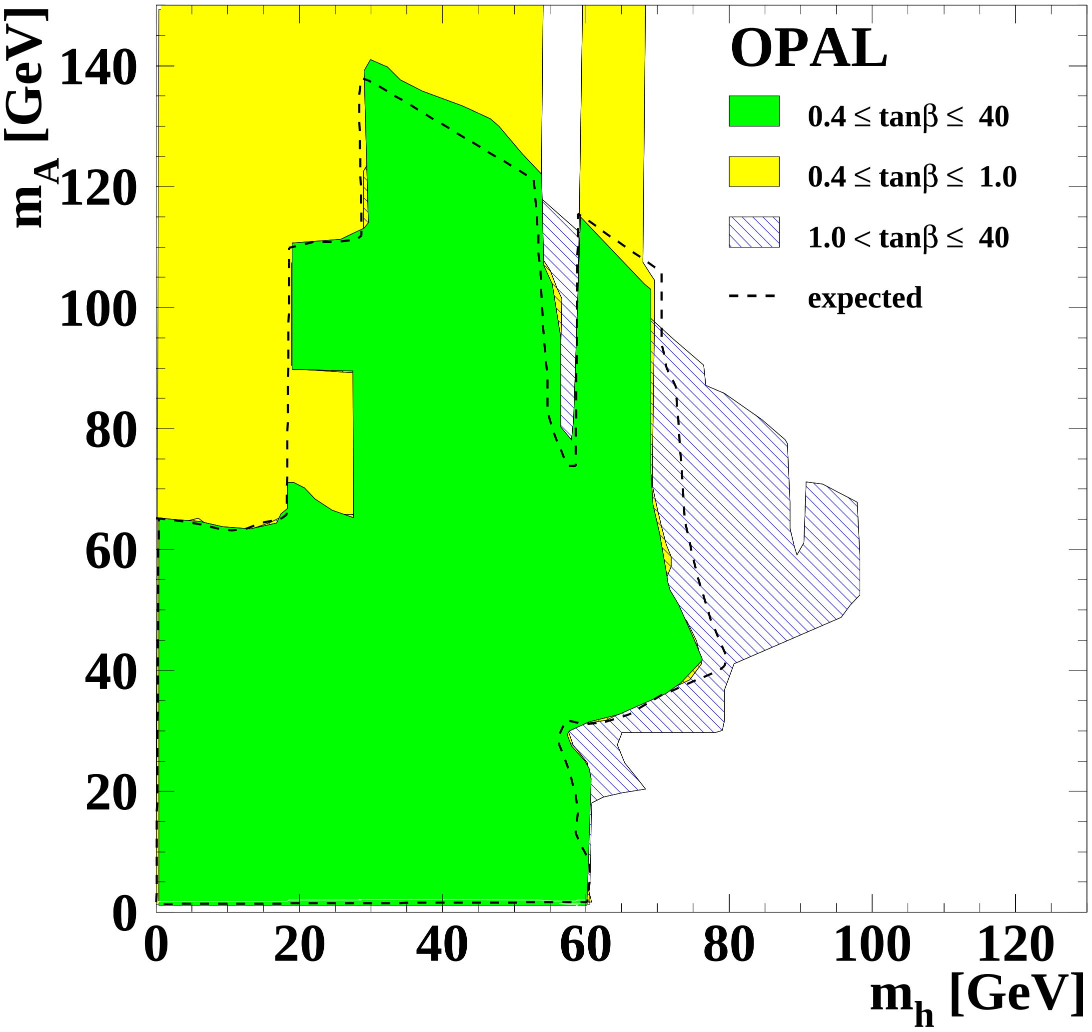

Figure 9: Excluded ($m_{\rm A}$, $m_{\rm h}$) region for $-\pi/2 \leq \alpha \leq 0$, together with the expected exclusion limit. A particular ($m_{\rm A}$, $m_{\rm h}$) point is excluded at 95% CL if it is excluded for $0.4 \leq \tan\beta \leq 40$ (darker grey region), $0.4 \leq \tan\beta \leq 1.0$ (lighter grey region) and $1.0 < \tan\beta < 40$ (hatched region). Expected exclusion limits for $0.4 \leq \tan\beta \leq 40$ are shown as a dashed line.

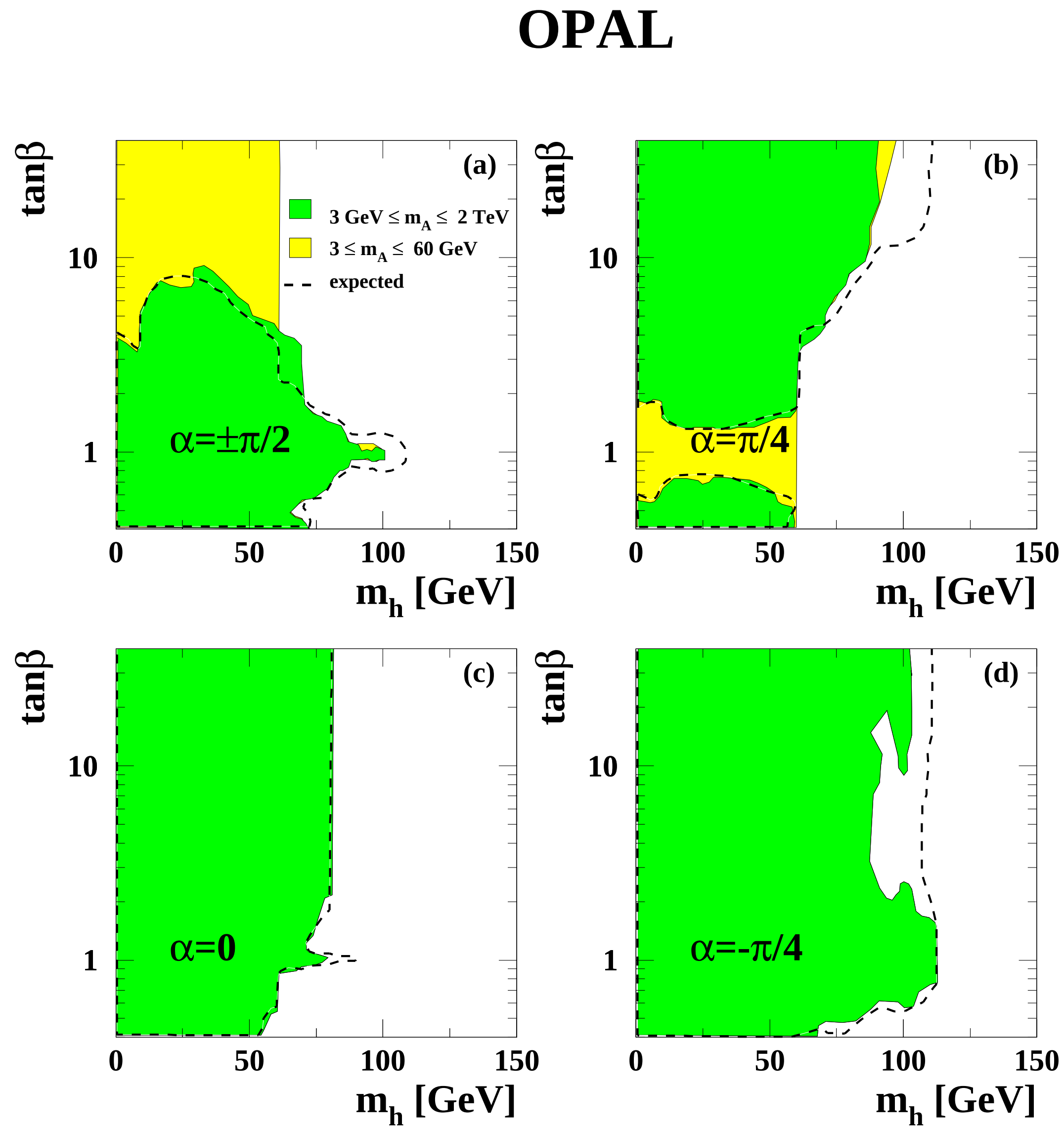

Figure 10: Excluded regions in the (tanβ, m_{h}) plane, (a)–(d), for α= $\pm\pi/2$, $\pi/4$, 0 and $-\pi/4$, respectively, together with the expected exclusion limits. A particular (m_{h}, tanβ, α) point is excluded at 95% CL if it is excluded for all scanned values of m_{A}. The two regions shown correspond to the whole domain 3 GeV $\leq m_{\mathrm{A}} \leq$ 2 TeV (darker grey area) and a restricted domain for which 3 $\leq$ m_{A} $\leq$ 60 GeV (lighter grey area). The exclusion regions for m_{A} $\leq$ 60 GeV entirely contain the 3 GeV $\leq m_{\mathrm{A}} \leq$ 2 TeV excluded areas. Expected exclusion limits are shown for 3 GeV $\leq$ $m_{\mathrm{A}} \leq$ 2 TeV (dashed line).

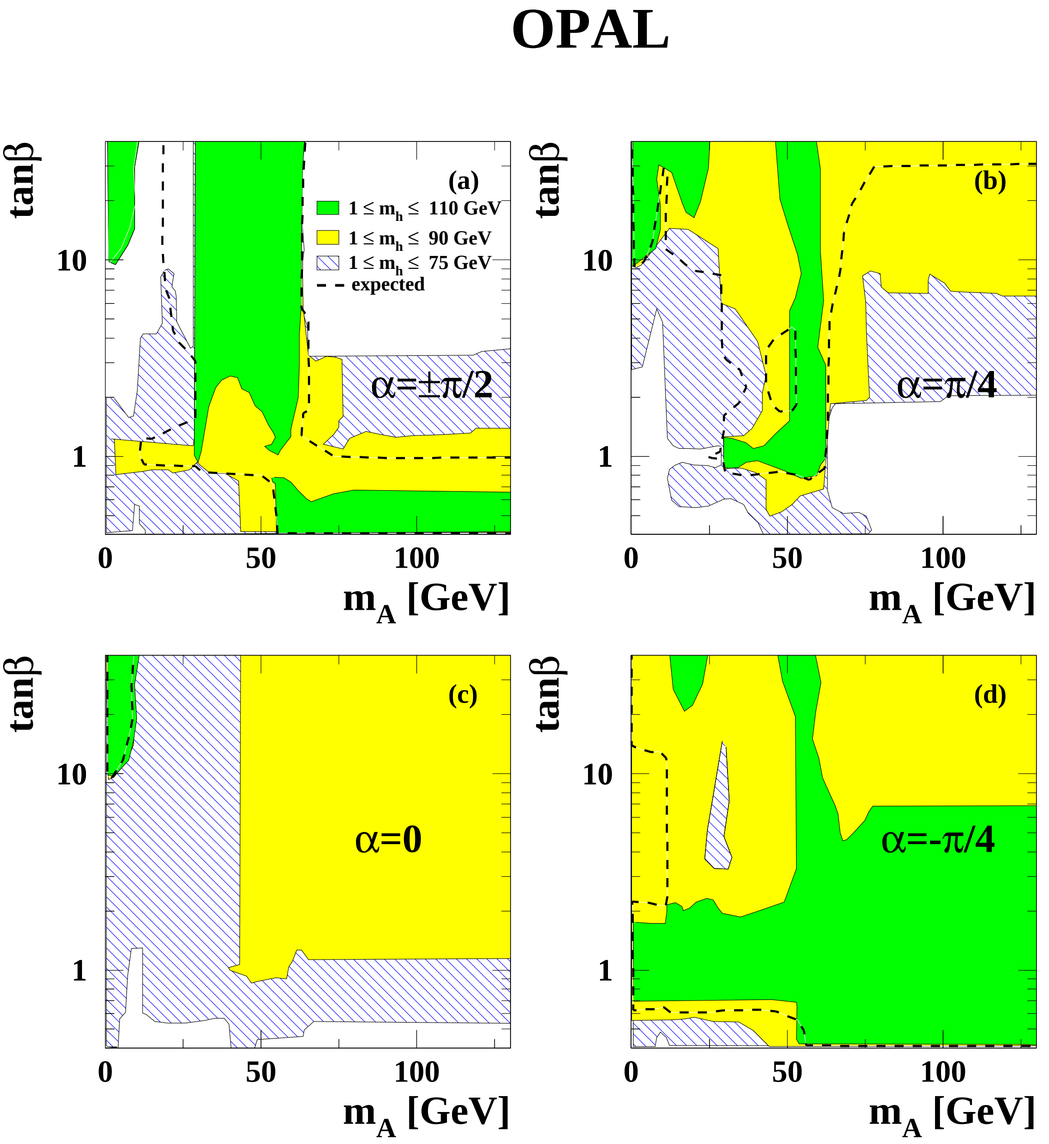

Figure 11: Excluded regions in the (m_{A}, tanβ) plane, (a)–(d), for α= $\pm\pi/2$, $\pi/4$, 0 and $-\pi/4$, respectively, together with the calculated expected exclusion limits. A particular (m_{A}, tanβ, α) point is excluded at 95% CL if it is excluded for all scanned values of m_{h}. The three contours correspond to $1 \leq m_{\mathrm{h}} \leq 110$ GeV (darker grey area) and $1 \leq m_{\mathrm{h}} \leq 90$ GeV (lighter grey area). Expected exclusion limits are shown for $1 \leq m_{\mathrm{h}} \leq 110$ GeV (dashed line).

References

[1] P. Higgs, Phys. Lett. **12**, 132 (1964).

[2] F. Englert and R. Brout, Phys. Rev. Lett. **13**, 321 (1964).

[3] G.S. Guralnik, C.R. Hagen and T.W.B. Kibble, Phys. Rev. Lett. **13**, 585 (1964).

[4] W. Hollik, Z. Phys **C32**, 291 (1986).

[5] W. Hollik, Z. Phys **C37**, 569 (1988).

[6] OPAL Collaboration, G. Abbiendi *et al.*, Eur. Phys. J. **C18**, 425 (2001).

[7] J.F. Gunion, H.E. Haber, G.L. Kane and S. Dawson, *The Higgs Hunter's Guide*, Addison-Wesley Publishing Company, 1990.

[8] P. Fayet, Nucl. Phys. **B90**, 104 (1975).

[9] J.F. Gunion and H.E. Haber, Nucl. Phys. **B278**, 449 (1986).

[10] OPAL Collaboration, K. Ahmet *et al.*, Nucl. Instr. and Meth. **A305**, 275 (1991).

[11] S. Anderson *et al.*, Nucl. Instr. and Meth. **A403**, 326 (1998).

[12] B.E. Anderson *et al.*, IEEE Transactions on Nuclear Science **41**, 845 (1994).

[13] OPAL Collaboration, K. Ackerstaff *et al.*, Phys. Lett. **B391**, 221 (1997).

[14] OPAL Collaboration, G. Abbiendi *et al.*, Eur. Phys. J. **C26**, 479 (2003).

[15] N. Brown and W.J. Stirling, Phys. Lett. **B252**, 657 (1990);
S. Catani *et al.*, Phys. Lett. **B269**, 432 (1991);
S. Bethke, Z. Kunszt, D. Soper and W.J. Stirling, Nucl. Phys. **B370**, 310 (1992);
N. Brown and W.J. Stirling, Z. Phys. **C53**, 629 (1992).

[16] P. Janot and G. Ganis, `HZHA` generator, *Physics at LEP2,* **CERN 96-01, Vol.2**, 309 (1996).

[17] S. Jadach, B.F.L. Ward and Z. Wąs, Comp. Phys. Comm. **130**, 260 (2000).

[18] S. Jadach, W. Płaczek, and B.F.L. Ward, *Physics at LEP2,* **CERN 96-01, Vol.2**, 286 (1996).

[19] M. Skrzypek *et al.*, Phys. Lett. **B372**, 289 (1996).

[20] J. Fujimoto *et al.*, Comp. Phys. Comm. **100**, 128 (1997).

[21] T. Sjöstrand, Comp. Phys. Comm. **82**, 74 (1994).

[22] G. Marchesini *et al.*, Comp. Phys. Comm. **67**, 465 (1992).

[23] J. Allison *et al.*, Nucl. Instr. and Meth. **A317**, 47 (1992).

[24] The LEP Collaborations ALEPH, DELPHI, L3 and OPAL, the LEP Electroweak Working Group and SLD Heavy Flavour and Electroweak Groups, **CERN-EP-2003-091** and hep-ex/0312023 (2003).

[25] OPAL Collaboration, K. Ackerstaff *et al.*, Eur. Phys. J. **C2**, 441 (1998).

[26] G. Hanson *et al.*, Phys. Rev. Lett. **35**, 1609 (1975);
G. Parisi, Phys. Lett. **B74**, 65 (1978).

[27] ALEPH Collaboration, R. Barate *et al.*, Phys. Lett. **B447**, 336 (1999).

[28] F.A. Berends, R. Pittau and R. Kleiss, Comp. Phys. Comm. **85**, 437 (1995).

[29] S. Catani and M.H. Seymour, **CERN-TH/96-28** (1996).

[30] A.L. Read, Nucl. Instr. Meth. **A425**, 357 (1999).

[31] M.W. Grünewald and G. Passarino *et al.*, hep-ph/0005309 (2000).

[32] T. Junk, Nucl. Instr. and Meth. **A434**, 435 (1999).

[33] A. Read, in *1st Workshop on Confidence Limits*, **CERN-2000-005** (2000) .

[34] OPAL Collaboration, G. Abbiendi *et al.*, **CERN-EP-2003-081**, *Accepted by Phys. Letts. B* (2003).

[35] OPAL Collaboration, G. Abbiendi *et al.*, **CERN-EP-PH-2004-020**, *Accepted by Eur. Phys. J.* (2004).

[36] OPAL Collaboration, G. Abbiendi *et al.*, Eur. Phys. J. **C27**, 483 (2003).

[37] J. Ellis and R. Peccei (editors), *Physics at LEP*, G. Altarelli *et al.*, **CERN 86-02, Vol. 1**, 203 (1986).

[38] OPAL Collaboration, K. Ackerstaff *et al.*, Eur. Phys. J. **C5**, 19 (1998).

[39] OPAL Collaboration, G. Abbiendi *et al.*, Eur. Phys. J. **C27**, 311 (2003).

[40] OPAL Collaboration, R. Akers *et al.*, Eur. Phys. J. **C23**, 397 (2002).

[41] OPAL Collaboration, P.D. Acton *et al.*, Phys. Lett. **B268**, 122 (1991).

[42] M. Krawczyk, J. Zochowski and P. Mättig, Eur. Phys. J. **C8**, 495 (1999).